A&A 627, A107 (2019)
https://doi.org/10.1051/0004-6361/201935536

Astronomy & Astrophysics

CO observations of major merger pairs at $z = 0$: molecular gas mass and star formation⋆

Ute Lisenfeld[1,2], Cong Kevin Xu[3,4], Yu Gao[5], Donovan L. Domingue[6], Chen Cao[7,8], Min S. Yun[9], and Pei Zuo[10]

[1] Departamento de Física Teórica y del Cosmos, Universidad de Granada, Spain
e-mail: ute@ugr.es
[2] Instituto Carlos I de Física Téorica y Computacional, Facultad de Ciencias, 18071 Granada, Spain
[3] National Astronomical Observatories, Chinese Academy of Sciences, 1000012 Beijing, PR China
[4] South American Center for Astronomy, CAS, Camino El Observatorio 1515, Las Condes, Santiago, Chile
[5] Purple Mountain Observatory, Chinese Academy of Sciences, 2 West Beijing Road, 210008 Nanjing, PR China
[6] Georgia College & State University, CBX 82, Milledgeville, GA 31061, USA
[7] School of Space Science and Physics, Shandong University, 264209 Weihai, Shandong, PR China
[8] Shandong Provincial Key Laboratory of Optical Astronomy & Solar-Terrestrial Environment, 264209 Weihai, Shandong, PR China
[9] Department of Astronomy, University of Massachusetts, Amherst, MA 01002, USA
[10] Kavli Institute for Astronomy and Astrophysics, Peking University, 5 Yiheyuan Road, Haidian District, 100871 Beijing, PR China

Received 25 March 2019 / Accepted 28 May 2019

ABSTRACT

We present CO observations of 78 spiral galaxies in local merger pairs. These galaxies represent a subsample of a K_s-band-selected sample consisting of 88 close major-merger pairs (HKPAIRs), 44 spiral–spiral (S+S) pairs, and 44 spiral–elliptical (S+E) pairs, with separation $< 20\,h^{-1}$ kpc and mass ratio < 2.5. For all objects, the star formation rate (SFR) and dust mass were derived from *Herschel* PACS and SPIRE data, and the atomic gas mass, $M_{\rm HI}$, from the Green Bank Telescope HI observations. The complete data set allows us to study the relation between gas (atomic and molecular) mass, dust mass, and SFR in merger galaxies. We derive the molecular gas fraction ($M_{\rm H_2}/M_*$), molecular-to-atomic gas mass ratio ($M_{\rm H_2}/M_{\rm HI}$), gas-to-dust mass ratio and SFE (= SFR/$M_{\rm H_2}$) and study their dependences on pair type (S+S compared to S+E), stellar mass, and the presence of morphological interaction signs. We find an overall moderate enhancement (∼2×) in both molecular gas fraction ($M_{\rm H_2}/M_*$) and molecular-to-atomic gas ratio ($M_{\rm H_2}/M_{\rm HI}$) for star-forming galaxies in major-merger pairs compared to non-interacting comparison samples, whereas no enhancement was found for the SFE nor for the total gas mass fraction ($(M_{\rm HI} + M_{\rm H_2})/M_*$). When divided into S+S and S+E, low mass and high mass, and with and without interaction signs, there is a small difference in SFE, a moderate difference in $M_{\rm H_2}/M_*$, and a strong difference in $M_{\rm H_2}/M_{\rm HI}$ between subsamples. For the molecular-to-atomic gas ratio $M_{\rm H_2}/M_{\rm HI}$, the difference between S+S and S+E subsamples is 0.55 ± 0.18 dex and between pairs with and without interaction sign 0.65 ± 0.16 dex. Together, our results suggest that (1) star formation enhancement in close major-merger pairs occurs mainly in S+S pairs after the first close encounter (indicated by interaction signs) because the HI gas is compressed into star-forming molecular gas by the tidal torque; and (2) this effect is much weakened in the S+E pairs.

Key words. galaxies: evolution – galaxies: general – galaxies: interactions – galaxies: starburst – ISM: molecules

1. Introduction

Gravitational interaction is an important process for the evolution of galaxies in clusters (Dressler 1980; Moore et al. 1996), groups (Hickson et al. 1992; Lisenfeld et al. 2017), triplets (Duplancic et al. 2015; Argudo-Fernández et al. 2015) and pairs (Ellison et al. 2010; Argudo-Fernández et al. 2015). It is now well established that galaxy interactions in pairs can cause an enhancement of the star formation rate (SFR). The size of the enhancement depends on parameters of the galaxies (mass ratio, gas fraction), on the orbital parameters of the interacting galaxies (e.g. Kennicutt et al. 1987; Xu et al. 1990), and on the phase of the interaction (e.g. Di Matteo et al. 2007; Cox et al. 2008; Scudder et al. 2012). The largest enhancements of the SFR occur in equal-mass mergers (major mergers) after the first pericentre and, much stronger, during coalescence (e.g. Nikolic et al. 2004; Scudder et al. 2012). In most cases the SFR enhancement is only moderate (less than a factor of 5 in 85% of cases; Di Matteo et al. 2008), but when all parameters are favourable (gas rich, equal-mass galaxies during coalescence) short episodes of very high SFR can occur, the most extreme examples being (ultra) luminous infrared galaxies ((U)LIRGs; e.g. Sanders & Mirabel 1996; Ellison et al. 2013).

Simulations of galaxy mergers have helped to improve our understanding of the processes that affect the SFR during a merger. It has long been recognized that tidal forces can produce an increase of the SFR (see Barnes & Hernquist 1992). Gravitational torques produced by asymmetric tidal forces cause the gas at large radii to lose angular momentum and fall into the central regions where the high gas surface density produces a central

⋆ A copy of the reduced spectra and full Tables 1 and 2 are available at the CDS via anonymous ftp to cdsarc.u-strasbg.fr (130.79.128.5) or via http://cdsarc.u-strasbg.fr/viz-bin/qcat?J/A+A/627/A107

starburst. High-resolution simulations have shown that, in addition, changes in the substructure of the interstellar medium (ISM) can favour the collapse of molecular clouds and thus enhance the SFR (Teyssier et al. 2010). Parsec-resolution simulations by Renaud et al. (2014) led to the finding that during a typical galaxy merger tidal compression can increase and modify turbulence, leading to an excess of dense gas and an enhancement in SF activity and the SF efficiency (SFE = SFR/$M_{\rm H_2}$).

In order to observationally better understand the questions of when and how SF is enhanced during the merging process, Domingue et al. (2009) selected a sample of close major mergers based on the K_s-band (KPAIR sample). Xu et al. (2010) studied the specific SFR (sSFR = SFR/M_*) enhancement in this sample and found enhancement in galaxies in spiral–spiral (S+S) pairs, but none in spiral–elliptical (S+E) pairs. This result was confirmed by Cao et al. (2016) for an extended sample (H-KPAIR sample) based on *Herschel* PACS and SPIRE data. These data allowed these latter authors to derive the SFR and dust mass, which can be used as an indicator of the total gas mass, assuming a constant dust-to-gas mass ratio. They found an increase in the $\rm SFE_{gas}$ (= SFR/$M_{\rm gas}$) of spirals in S+S pairs, whereas the value in spirals in S+E pairs is the same as for a control sample. The difference between the gas fraction ($M_{\rm gas}/M_*$) in star forming galaxies in S+S and S+E pairs is weak (~40%) and insignificant, indicating that the amount of gas is not the reason for this difference. Using WISE and *Herschel* data, Domingue et al. (2016) found that spirals in S+S pairs exhibit a significant enhancement in the interstellar radiation field and dust temperature, while spirals in S+E pairs do not. Zuo et al. (2018) observed the sample in HI with the Green Bank Telescope and found a difference in $\rm SFE_{HI}$ (= SFR/$M_{\rm HI}$) between S+S and S+E pairs.

Molecular gas is more closely related to the process of SF than atomic hydrogen. The SFR can be enhanced by a larger amount of molecular gas from which stars form, or by making the process of star formation from gas more efficient (i.e. increasing SFE), for example by increasing the gas density. Both scenarios can be distinguished observationally by measuring the molecular gas mass (compared to the stellar or atomic gas mass) and the SFE. The role of the molecular gas in galaxy interactions has been investigated in numerous studies. There is a general consensus that the molecular gas content is enhanced in interacting galaxies. This has already been seen in the first studies with samples ranging from ~10 to 1000 galaxies (Braine & Combes 1993; Combes et al. 1994; Casasola et al. 2004), and has been confirmed in more recent studies. Violino et al. (2018) found for a small sample of nine nearby galaxies, which they compared to a well-matched comparison sample, that both the molecular gas fraction ($M_{\rm H_2}/M_*$) and the SFE are enhanced in the interacting sample. Both parameters are however consistent with non-mergers of similarly enhanced SFR. Pan et al. (2018) investigated a sample of 58 pairs and found an enhancement of the SFR, SFE, $M_{\rm H_2}$ and $M_{\rm H_2}/M_*$. Whereas the enhancement of the SFR, $M_{\rm H_2}$, and $M_{\rm H_2}/M_*$ increases with decreasing pair separation, the SFE is only enhanced in close (separation < 20 kpc) pairs and equal-mass systems. An enhancement of the SFE was found in the earlier studies only in strongly interacting galaxies (Solomon & Sage 1988; Sofue et al. 1993) whereas more-weakly interacting pairs did not show any enhancement (Solomon & Sage 1988). No enhancement in the SFE was found in studies with mixed interacting samples (Combes et al. 1994; Casasola et al. 2004), whereas the more recent studies (Violino et al. 2018; Pan et al. 2018) did find a small ($\lesssim$ factor of 2) increase in the SFE.

In the present paper we present new CO data for a subsample of H-KPAIR, which includes only close major mergers ($r < 20\,h^{-1}$ kpc, mass ratio < 2.5). These data allow us to calculate and analyse the molecular gas content in a homogenous sample with a large ancillary data set. Together with the data from Cao et al. (2016) and Zuo et al. (2018) we now have a complete data set to study the relation between the cold ISM (atomic, molecular gas, and dust) and SF. This sample allows us to analyse this relation as a function of pair type (S+S or S+E), stellar mass, and interaction stage classified by morphology. The goal of the present paper is to better understand how SF is enhanced in the merging process, and to distinguish the role played by the gas, in particular the molecular component.

Throughout this paper, we adopt the Λ-cosmology with $\Omega_{\rm m} = 0.3$ and $\Omega_\Lambda = 0.7$ and $H_0 = 70\,{\rm km\,s^{-1}\,Mpc^{-1}}$.

2. The sample

The local galaxy pair sample used in this work was constructed from the KPAIR sample which is a complete and unbiased K_s-band (2.16 μm)-selected sample of 170 close major-merger galaxy pairs (see details in Domingue et al. 2009; Xu et al. 2012). Their projected distance, r, is in the range of 5–20 h^{-1} kpc and the mass ratio of the pair components is ≤2.5. Cao et al. (2016) selected a subsample of 88 galaxy pairs for observations with *Herschel* from this sample (hereafter H-KPAIR) by excluding (i) elliptical+elliptical (E+E) pairs; (2) pairs with only one measured redshift, and (3) pairs with recession velocities <2000 km s^{-1}. This sample includes 44 spiral+spiral (S+S) and 44 spiral+elliptical (S+E) pairs. All galaxies have $z < 0.1$ with a median of $z = 0.04$. The galaxies were classified by visual inspection as not showing any merger signs (labelled "JUS"), galaxies with interactions signs (labelled "INT"), and pairs in the process of merging (labelled "MER").

From the H-KPAIR sample we selected a subsample of spirals in both S+S and S+E pairs that were observed in CO(1–0). We did not observe elliptical galaxies because they generally have a low molecular gas content and are not actively star forming. In order to enhance the probability of detection we restricted the sample to close-by (redshift < 0.055) and relatively infrared-bright objects, i.e. detected at 70 μm. Following these criteria, we observed 78 spiral galaxies out of the H-PAIR sample, 55 of them in S+S pairs and 23 in S+E pairs.

Among 176 galaxies in the HKPAIR sample, 12 (8 of them with CO data) contain an AGN according to optical spectroscopy (Cao et al. 2016). Most of them do not show any significant difference in their mid- or far-infrared (FIR) emission compared to other galaxies in the sample. Only two galaxies, J13151726+4424255 and J12115648+4039184, show possible AGN contributions in their WISE colours (Domingue et al. 2016). This is consistent with Nordon et al. (2012) and Lam et al. (2013) who found that for most AGN-hosting galaxies, the contribution from AGN to the infrared luminosity is insignificant. The inclusion of these AGNs does not affect our main results.

3. Data

3.1. CO observations and data reduction

Observations were carried out between July 2015 and May 2018 with the Institut de Radioastronomie Milimetrique (IRAM) 30 m telescope on Pico Veleta. We observed the redshifted ^{12}CO(1–0) and ^{12}CO(2–1) lines in parallel in the central position of each galaxy. We used the dual polarization receiver EMIR in combination with the autocorrelator FTS at a frequency resolution of 0.195 MHz (providing a velocity resolution of ~0.5 km s^{-1}

at CO(1–0)) and with the autocorrelator WILMA with a frequency resolution of 2 MHz (providing a velocity resolution of ~5 km s^{-1} at CO(1–0)). The observations were done in wobbler switching mode with a wobbler throw between 40 and 120″ in azimuthal direction. The wobbler throw was chosen individually in order to ensure that the off-position was well outside the partner galaxy.

The broad bandwidth of the receiver (16 GHz) and backends (8 GHz for the FTS and 4 GHz for WILMA) allow the observations of galaxies to be grouped into similar redshifts. We organised the groups giving priority to the CO(1–0) line, and accepted that in some cases CO(2–1) was not covered by the narrower velocity bandwidth of the E230 receiver. The observed frequencies, taking into account the redshift of the objects, range between 108 and 113 GHz for CO(1–0) and between 218 and 227 GHz for CO(2–1). Each object was observed until it was detected with a S/N ratio of at least 5 or until a root-mean-square noise (rms) of <3 mK (T_A^*) was achieved for a velocity resolution of 20 km s^{-1}. The integration times per object ranged between 15 and 100 min. Pointing was monitored on nearby quasars every 60–90 min. During the observation period, the weather conditions were generally good, with a pointing accuracy better than 3–4″. The mean system temperature for the observations was 170 K for CO(1–0) and 360 K for CO(2–1) on the T_A^* scale. At 115 GHz (230 GHz), the IRAM forward efficiency, $F_{\rm eff}$, was 0.95 (0.91) and the beam efficiency, $B_{\rm eff}$, was 0.77 (0.58). The half-power beam size for CO(1–0) ranges between 21.8″(for 113 GHz) and 22.8″(for 108 GHz), and the values for CO(2–1) are a factor of two smaller. All CO spectra and luminosities are presented on the main beam temperature scale ($T_{\rm mb}$) which is defined as $T_{\rm mb} = (F_{\rm eff}/B_{\rm eff}) \times T_A^*$.

The data were reduced in the standard way via the CLASS software in the GILDAS package[1]. We first discarded poor scans and then subtracted a constant or linear baseline. Some observations taken with the FTS backend were affected by platforming, that is the baseline level changed abruptly at one or two positions along the band. This effect could be reliably corrected because the baselines in between these (clearly visible) jumps were linear and could be subtracted from the different parts individually, using the *FtsPlatformingCorrection5.class* procedure provided by IRAM. We then averaged the spectra and smoothed them to resolutions of 21 km s^{-1}.

We present the detected spectra in the appendix (Figs. A.1 and A.2). For each spectrum, we visually determined the zero-level line widths, if detected. The velocity-integrated spectra were calculated by summing the individual channels in between these limits. For non-detections we set an upper limit as

$$I_{\rm CO} < 3 \times {\rm rms} \times \sqrt{\delta {\rm V}\, \Delta V}, \quad (1)$$

where δV is the channel width (in kilometres per second), ΔV the zero-level line width (in kilometres per second), and rms the root mean square noise (in Kelvin). For the non-detections, we assumed a line width of $\Delta V = 400$ km s^{-1} which is close to the mean velocity width found for CO(1–0) in the sample (mean $\Delta V = 435$ km s^{-1} with a standard deviation of 210 km s^{-1}). We treated tentative detections, with a S/N ratio in the range 3–5, as upper limits in the statistical analysis. The results of our CO(1–0) observations are listed in Table 1. In addition to the statistical error of the velocity-integrated line intensities, a calibration error of 15% for CO(1–0) and 30% for CO(2–1) has to be taken into account. These errors were determined by comparing the observations of several strong sources (J0823+2120A, J0823+2120B, J1315+4424a and J1444+1207A) on different days.

[1] http://www.iram.fr/IRAMFR/GILDAS

3.2. Aperture correction and molecular gas mass

We only observed the galaxies in their central pointing, which in most cases covers only a fraction of the entire galaxy. This fraction is furthermore different for each galaxy depending on its size. Therefore, we need to apply a correction for emission outside the beam. We carried out this aperture correction in the same way as described in Lisenfeld et al. (2011), assuming an exponential distribution of the CO flux:

$$S_{\rm CO}(r) = S_{\rm CO,center} \propto \exp(-r/r_{\rm e}), \quad (2)$$

where $S_{\rm CO,center}$ is the CO(1–0) flux in the central position and derived from the measured $I_{\rm CO}$ applying the $T_{\rm mB}$ -to-flux conversion factor of the IRAM 30 m telescope (5 Jy/K). Lisenfeld et al. (2011) derived a scale length of $r_{\rm e} = 0.2 \times r_{25}$, where r_{25} is the major optical isophotal radius at 25 mag arcsec^{-2}, from different studies of local spiral galaxies (Nishiyama et al. 2001; Regan et al. 2001; Leroy et al. 2008) and from their own CO data. Very similar values for $r_{\rm e}/r_{25}$ were found by Boselli et al. (2014; $r_{\rm e}/r_{25} \sim 0.2$) and Casasola et al. (2017; $r_{\rm e}/r_{25} = 0.17 \pm 0.03$) from an analysis of nearby mapped galaxies.

For our sample r_{25} is only available for 45 out of the 178 HKPAIR galaxies. In addition, an isophotal radius such as r_{25} can be affected by confusion in close pairs. We therefore use the Kron radius, $r_{\rm kron}$, derived from the K_s-band and obtained from the 2MASS archive. We compared r_{25} and $r_{\rm kron}$ for the 45 galaxies where both radii are available and obtained a mean value of $r_{25}/r_{\rm kron} = 1.33$, with a standard deviation of 0.66, and a median value of 1.2. The large scatter is mostly due to a few objects with a relatively high $r_{25}/r_{\rm kron}$ ($\gtrsim$2) where r_{25} is most likely affected by confusion. We therefore use the median value of $r_{25}/r_{\rm kron} = 1.2$ as the more robust estimate. Thus, we adopt $r_{\rm e} = 0.2 \times 1.2 \times r_{\rm kron} = 0.24 \times r_{\rm kron}$ in Eq. (2) and use this distribution to calculate the expected CO flux from the entire disk, $S_{\rm CO,tot}$, taking the galaxy inclination into account, by 2D integration over the exponential galaxy disk (see Lisenfeld et al. 2011, for more details). We derive the inclination of the galaxy from the K_s-band major-to-minor axis ratio, obtained from the 2MASS archive. Boselli et al. (2014) generalized this method to three dimensions by taking the finite thickness of galaxy disks into account. Except for edge-on galaxies ($i > 80°$) the 3D method gives basically the same result as the 2D approximation, and also for edge-on galaxies the difference is <5% for $z_{\rm CO}/\Theta < 0.1$ ($z_{\rm CO}$ being the scale height of the CO perpendicular to the disk and Θ the beam size). We therefore consider the 2D aperture correction to be sufficient.

The resulting aperture correction factors, $f_{\rm aper}$, defined as the ratio between $S_{\rm CO,center}$ and the total aperture-corrected flux $S_{\rm CO,tot}$, lie between 1.0 and 5.0 with a mean (median) value of 1.5 (1.4). The values for the extrapolated molecular gas mass and $f_{\rm aper}$ are listed in Table 2.

We calculate the molecular gas mass from the CO(1–0) luminosity, $L'_{\rm CO}$ (following Solomon et al. 1997), derived as:

$$L'_{\rm CO}[{\rm K\,km\,s^{-1}\,pc^{-2}}] = 3.25 \times 10^7\, S_{\rm CO,tot} \nu_{\rm rest}^{-2} D_{\rm L}^2 (1+z)^{-1}, \quad (3)$$

where $S_{\rm CO,tot}$ is the aperture-corrected CO line flux (in Jy km s^{-1}), $D_{\rm L}$ is the luminosity distance in Mpc, z the redshift, and $\nu_{\rm rest}$ is the rest frequency of the line in gigahertz. We then calculate the molecular gas mass as

$$M_{\rm H_2}[M_\odot] = \alpha_{\rm CO} L'_{\rm CO}. \quad (4)$$

Table 1. Velocity-integrated CO intensities.

Galaxy name	Pair name	rms [a] [mK]	$I_{CO(1-0)}$ [b] [K km s^{-1}]	$\Delta V_{CO(1-0)}$ [c] [km s^{-1}]	rms [a] [mK]	$I_{CO(2-1)}$ [b],[d] [K km s^{-1}]	$\Delta V_{CO(2-1)}$ [c] [km s^{-1}]
J00202580+0049350	J0020+0049	6.19	6.54 ± 0.47	280	27.16	12.78 ± 2.06	275
J01183417–0013416	J0118–0013	3.49	6.86 ± 0.38	558	–	–	–
J01183556–0013594	J0118–0013	3.93	2.63 ± 0.22	150	–	–	–
J02110638–0039191	J0211–0039	4.32	7.53 ± 0.43	465	13.24	22.42 ± 1.31	465
J03381222+0110088	J0338+0109	3.00	4.07 ± 0.27	380	9.92	8.59 ± 0.80	310
...	...	...	...	...	...	...	...

Notes. [*]Tentative detections. [a]Root-mean-square noise at a velocity resolution of 21 km s^{-1}. [b]Velocity integrated intensity of the CO(1–0) and the CO(2–1) lines. [c]Zero-level line width. The uncertainty is roughly given by the velocity resolution (21 km s^{-1}). [d]For some objects the bandwidth does not entirely cover the expected CO(2–1) frequency meaning that no value for $I_{CO(2-1)}$ can be given. The full table is available at the CDS.

Table 2. Molecular gas mass.

Galaxy name	Distance [Mpc]	$\log(M_{H_2})$ [a] [$M_\odot$]	f_{aper} [b]
J00202580+0049350	64.4	9.44	2.63
J01183417–0013416	200.9	10.10	1.22
J01183556–0013594	201.7	9.71	1.29
J02110638–0039191	77.0	9.52	1.92
J03381222+0110088	172.9	9.80	1.38
...	...	...	...

Notes. [a]Cold molecular gas mass, extrapolated from the central pointing to the entire disk, calculated as described in Sect. 3.2. [b]Aperture correction $f_{aper} = M_{H_2}/M_{H_2,center}$. The full table is available at the CDS.

We adopt the Galactic value ($\alpha_{CO} = \alpha_{CO,Gal} = 3.2 M_\odot/(\mathrm{K\,km\,s^{-1}\,pc^{-2}})$; Bolatto et al. 2013), and do not include helium or heavy metals in the mass. This conversion factor corresponds to $X = N_{H_2}/I_{CO} = 2 \times 10^{20}\,\mathrm{cm^{-2}\,(K\,km\,s^{-1})^{-1}}$.

This empirical aperture correction could potentially introduce a bias in our analysis. We therefore investigated the distribution of f_{aper}, separate for S+S pairs and S+E pairs (Fig. 1). Two features are visible that are relevant to this problem. Firstly, for most of the objects the aperture correction is below 2 (91%, and 60% below 1.5) which means that possible errors introduced by this correction are small. Secondly, the distribution of f_{aper} for spirals in S+S and in S+E pairs is very similar and no features indicating the presence of a bias are obvious.

3.3. Dust emission, SFR, and stellar mass

All objects in our sample were imaged with the *Herschel* instruments PACS & SPIRE (Cao et al. 2016). These authors fitted the dust SED with the model of Draine et al. (2007) and derived the total IR luminosity, L_{IR}, as well as the dust mass from it. They calculated the SFR from L_{IR} using the expression given in Kennicutt (1998), adapted to a Kroupa IMF, as SFR ($M_\odot\,\mathrm{yr^{-1}}$) = 2.2×10^{-10} ($L_{IR}/L_\odot$). This derivation of the SFR misses the contribution from unobscured UV radiation, which is on the order of 20% for KPAIR galaxies (Yuan et al. 2012). It can also be affected by the contribution of old stars to the dust heating which is about 30% for spiral galaxies (Buat & Xu 1996) and even lower (0.17 ± 0.11, Buat et al. 2011) for massive, actively star-forming galaxies. Thus, both effects are not expected to be severe for our actively star-forming sample. In addition, since we use the same formalism for both the H-KPAIR and the AMIGA control sample, these possible biases are not expected to affect the results involving the SFR.

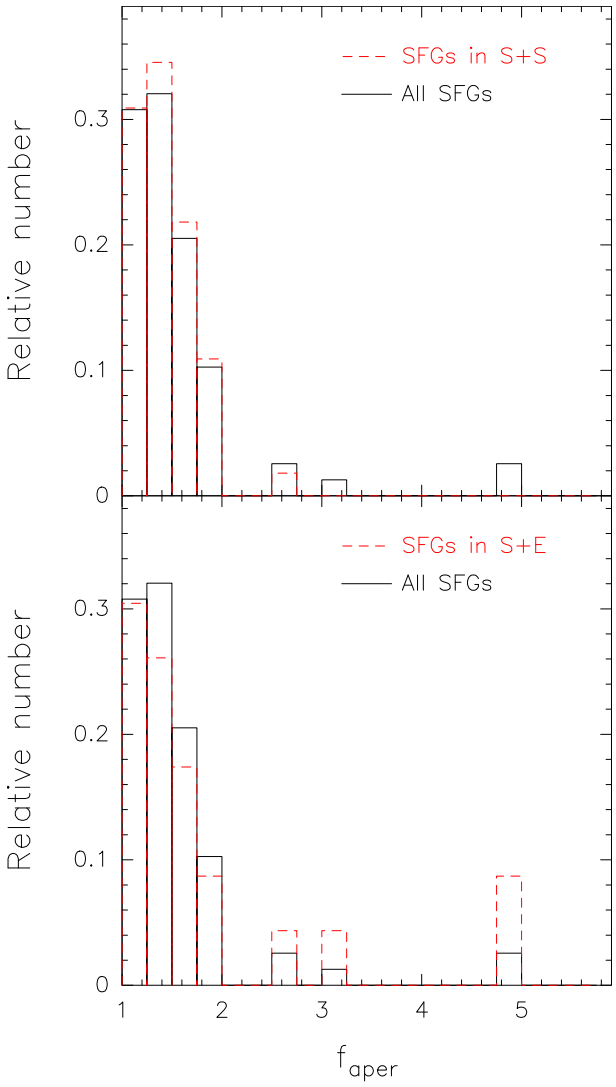

Fig. 1. Histogram of the distribution of the aperture correction, f_{aper}, for the different subsamples (red dashed line) compared to the full sample (full black line).

The stellar mass was calculated from the 2MASS K_s-band luminosity as $M_*(M_\odot) = 0.54\,L_K/L_{\odot,K}$ (Xu et al. 2012). The

near-infrared K_s band luminosity, mainly from old stars that dominate the stellar mass, is insensitive to dust extinction and star formation (Bell & de Jong 2001). The calibration for the conversion from L_K to M_* was derived from a comparison between L_K and M_* for normal galaxies in Kauffmann et al. (2013). We use the data provided by Cao et al. (2016), in particular the 70 μm PACS flux, SFR, dust, and stellar masses.

In addition, we derived the central 70 μm and K_s band fluxes within the IRAM CO(1–0) beam directly from the corresponding images in order to locally compare the SFR and stellar mass with the measured molecular gas mass in the centre of the galaxies, $M_{H_2,center}$. To achieve this, we multiplied the 70 μm image ($Im_{70\,\mu m}(x, y)$) and the K_s image ($Im_{K_s}(x, y)$) with the IRAM beam pattern (approximated as a normalized Gaussian beam) placed at the position where the CO beam was pointed during the observations (x_0, y_0):

$$Im_{70\,\mu m,beam}(x, y) = Im_{70\,\mu m}(x, y) \cdot \exp\left(\frac{(x - x_0)^2 + (y - y_0)^2)}{2\sigma^2}\right). \quad (5)$$

A corresponding expression is used for the K_s band image. The Gaussian standard deviation σ is related to the FWHM as $\sigma = FWHM/(2\sqrt{2\ln(2)}) = FWHM/2.35$. For the K_s band image we use the FWHM of the IRAM 30 m CO(1–0) beam, $FWHM = FWHM(\mathrm{IRAM}) = 21.34''(1 + z)$. For the 70 μm PACS image we use a slightly smaller value, $FWHM = \sqrt{FWHM(\mathrm{IRAM})^2 - FWHM(\mathrm{PACS})^2}$, in order to take into account the fact that the 70 μm image is already convolved to the PACS resolution, $FWHM(\mathrm{PACS}) \sim 6''$. From the resulting maps, $Im_{70\,\mu m,beam}(x, y)$ and $Im_{K_s,beam}(x, y)$, we then measured the total 70 μm flux, $S_{70\,\mu m,center}$, and K_s flux, $S_{K_s,center}$. We derived the central stellar mass within the IRAM beam from $S_{K_s,center}$ with the same relation as for the total stellar mass (see above). For the central SFR we assumed that it is well traced by the 70 μm emission and derived it as $SFR_{center} = SFR \cdot S_{70\,\mu m,center}/S_{70\,\mu m}$ where SFR and $S_{70\,\mu m}$ are the total SFR and 70 μm flux from Cao et al. (2016), respectively.

3.4. Atomic gas

We use the data for the atomic hydrogen (HI) content for 70 galaxy pairs (34 S+S pairs and 36 S+E pairs) from the H-KPAIR sample taken from Zuo et al. (2018). These authors observed 58 pairs with the Green Bank Telescope (GBT) and retrieved the data for an additional 12 pairs from the literature, giving a total of 70 pairs with HI data. We have CO data for 38 of these pairs.

4. Results

In the following section, we mainly study the relations between molecular gas mass, atomic gas mass, dust mass, stellar mass, and SFR. The main goal is to search for differences between spiral galaxies in S+S and S+E pairs and for trends with the stellar mass, and to investigate the influence of the stage of the merger process by distinguishing galaxies classified as not showing any merger signs (labelled "JUS") from galaxies with signs of interaction (labelled "INT") and pairs in the process of merging (labelled "MER"). Following Cao et al. (2016), we exclude from our sample galaxies with a low sSFR $< -11.3\,\mathrm{yr}^{-1}$ (seven objects and only one detection in CO(1–0)) which belong to the red sequence and are thus not actively star-forming galaxies.

Since the beam of the GBT (9′ for HI) is too large to separate the emission from the individual galaxies, the analysis taking into account HI data is done for each pair as a whole. For S+S pairs we sum the values for the SFR, stellar mass, dust mass, and molecular gas for both components. We then divide these values and the HI mass by two in order to obtain values typical for one galaxy. If only one member of a pair is observed in CO (two cases), we flag the total molecular gas mass and the total gas mass as a lower limit. For S+E pairs we assume, following Zuo et al. (2018), that the atomic gas is mostly associated to the spiral component. Zuo et al. (2018) tested this assumption using the gas mass derived from the dust mass (Cao et al. 2016) and found that the mean gas mass in elliptical galaxies is only about 10% of the total mass in a S+E pair. We thus make a 10% correction and assume that M_{HI} of the spiral component in S+E pairs is 90% of the M_{HI} observed in the pair. The other variables, M_{H_2}, M_*, SFR, and M_{dust} are taken for the spiral component only.

We list the mean and median values for different ratios, separated for the different groups, in Table 4. In this table, we present the values for the entire galaxies (or pairs). As a check, we also examined all relations involving M_{H_2}, M_* and SFR for the central values within the IRAM beam. We obtained very similar results, with the mean values agreeing within the errors. This supports the robustness of our conclusions.

4.1. Comparison sample

In order to search for differences between our merger sample and non-interacting galaxies, we need to compare our results to a suitable comparison sample. The comparison sample used in Cao et al. (2016) which was selected from the SDSS and matched to the HKPAIR sample does not include data for the molecular gas and can therefore only be used for a comparison of the SFR or M_{dust}, which is a good indicator for the total gas mass (e.g. Eales et al. 2012; Corbelli et al. 2012).

Different catalogues of non-interacting galaxies containing CO, HI, SFR, and M_* exist in the literature; for example the AMIGA sample of isolated galaxies (Verdes-Montenegro et al. 2005; Lisenfeld et al. 2011), the COLDGASS sample of mass-selected nearby galaxies (Saintonge et al. 2011a,b), and a catalogue of the ISM of normal galaxies (Bettoni et al. 2003). Here, we use the AMIGA and the COLD GASS sample for comparison because the CO observations for both samples have been taken with the IRAM 30m telescope and have been processed in a similar way as for our interacting sample. We present the relevant mean and median values in Table 3. We adapt all values to the Kroupa IMF, the Galactic α_{CO}, and do not include helium and heavy metals in the gas masses, and we limit the objects to those with sSFR $> -11.3\,\mathrm{yr}^{-1}$, as in our pair sample.

The AMIGA sample consists of 1050 local isolated galaxies (Verdes-Montenegro et al. 2005). Out of this sample, a volume-limited (recession velocities between 1500 and 5000 km s^{-1}) subsample of 173 objects possess CO data and their molecular gas properties were analysed in Lisenfeld et al. (2011). The CO data were observed, as in the present paper, for the central position of the galaxy and the total molecular mass was calculated with the same extrapolation procedure as in the present paper. In Lisenfeld et al. (2011), the K-band luminosities, L_K, are presented and we use them to calculate the stellar mass in the same way as here (see Sect. 3.3). Also, the SFR is calculated in a very similar way as here from the total FIR luminosity based on IRAS data, L_{IR}, following the expression from Kennicutt (1998). The AMIGA sample comprises a stellar mass range of $\log(M_*) \sim 9$–11 which extends to lower masses than our sample. Therefore, we recalculated all mean and median values restricting the sample to high-mass spirals ($M_* > 10^{10}\,M_\odot$),

and using the Kaplan-Meier estimator to take upper limits into account.

The COLD GASS galaxy sample (Saintonge et al. 2011a,b) is a mass-selected ($M_* > 10^{10}\,M_\odot$) local sample of approximately 350 galaxies. The HI fluxes were obtained from the GASS survey (Catinella et al. 2018). The COLD GASS sample matches the HKPAIR sample in stellar mass ($\log(M_*) \sim 10-11.4$). The CO (1–0) was observed with the IRAM 30 m telescope for the central position. In order to obtain the total CO flux, an aperture correction was derived by the authors based on CO maps of nearby spiral galaxies (Kuno et al. 2007) for which the impact of the observation with the IRAM beam was simulated for different redshifts. In this way, the flux that would be measured by a 22″ Gaussian beam ($S_{\rm CO-beam}$) was calculated and compared to the total flux of the maps, $S_{\rm tot}$. The dependence of the aperture correction factor $S_{\rm tot}/S_{\rm CO-beam}$ on the optical radius, d_{25}, was fitted and provided an aperture correction as a function of d_{25} (see Eq. (2) of Saintonge et al. 2011a). For galaxies with $d_{25} \geq 40''$ these latter authors improved the scatter in the relation between the aperture correction factor and d_{25} by performing an off-centre pointing along the major axis and used an empirical relation based on the ratio of the off-centre and central CO fluxes (see Eq. (3) of Saintonge et al. 2011a). The stellar mass and the SFR were calculated from optical/UV spectral energy distribution (SED) based on a Chabrier IMF, which is very similar to the Kroupa IMF used in the present paper. In order to match the COLD GASS sample to ours, we made two further restrictions: (i) We selected late-type galaxies based on the concentration index, C (the ratio of the r-band Petrosian radii encompassing 90% and 50% of the flux, $C = r_{90,r}/r_{50,r}$). We selected those galaxies with $C > 2.85$ corresponding to galaxies with morphological types of Sa or later (Yamauchi et al. 2005). (ii) We also excluded those galaxies that were found to be in pairs by Pan et al. (2018).

The results for the two comparison samples are reasonably consistent. The mean values have differences of less than 2σ except for the molecular gas fraction where the AMIGA sample has a mean value which is 0.22 ± 0.06 dex lower than that of the COLDGASS sample. The reason for this difference is not completely clear. The AMIGA sample was selected with strict isolation criteria and has a low molecular gas content (Lisenfeld et al. 2011) and a low SFR (Lisenfeld et al. 2007) compared to other samples. However, if this were the reason for the difference with COLDGASS, we would expect not only a difference in $M_{\rm H_2}/M_*$ but a similar difference in $M_{\rm H_2}/M_{\rm HI}$ which is not the case. In the following, we use the AMIGA sample for quantitative comparisons, but we note that all the conclusions are also valid compared to the COLDGASS sample.

Table 3. Mean and median values of the comparison samples.

Parameter	AMIGA mean median $n/n_{\rm up}$ [(a)]	ColdGASS mean median $n/n_{\rm up}$ [(a)]	Cao et al. (2016) mean median n [(a)]
$\log(M_{\rm H_2}/M_{\rm HI})$	-0.63 ± 0.06 -0.58 76/12	-0.49 ± 0.05 -0.46 81/10	
$\log(M_{\rm H_2}/M_*)$	-1.48 ± 0.05 -1.35 78/14	-1.26 ± 0.04 -1.20 168/15	
$\log(M_{\rm gas}/M_*)$	-0.77 ± 0.05 -0.71 77/13	-0.82 ± 0.04 -0.81 81/10	
$\log({\rm SFE})$	-9.07 ± 0.05 -9.13 62/7	-8.97 ± 0.04 -8.98 168/15	
$\log({\rm SFE_{gas}})$	-9.73 ± 0.05 -9.79 61/6	-9.63 ± 0.07 -9.66 81/10	-9.86 ± 0.05 [(b)] – 132/0

Notes. [(a)]Total number of galaxies (n) and number of upper limits ($n_{\rm up}$). [(b)]The value from Cao et al. (2016) is adapted to our mean gas-to-dust mass ratio of 155.

4.2. CO line ratio

In our sample we have 53 objects for which measurements for both $I_{\rm CO(1-0)}$ and $I_{\rm CO(2-1)}$ are available and which allow us to derived their line ratios. We show the relation between both lines in Fig. 2. We derive (taking upper limits in $I_{\rm CO(2-1)}$ into account) a mean value of $R_{21} = I_{\rm CO(2-1)}/I_{\rm CO(1-0)} = 1.5 \pm 0.1$. If we only take objects with detections in both $I_{\rm CO(1-0)}$ and $I_{\rm CO(2-1)}$ into account (42 galaxies) the mean value is $R_{21} = 1.7 \pm 0.1$. Both values are not aperture corrected.

To interpret R_{21} one has to consider, apart from the excitation temperature of the gas, two main parameters: the source size relative to the beam and the opacity of the molecular gas. For optically thick, thermalized emission with a point-like distribution we expect a ratio $R_{21} = \Theta^2_{\rm B(CO10)}/\Theta^2_{\rm B(CO21)} = 4$ (with $\Theta_{\rm B}$ being the FWHM of the beams). On the other hand, for a source that is more extended than the beams, we expect $R_{21} \sim 0.6-1$ for optically thick gas in thermal equilibrium, where R_{21} depends on the temperature of the gas, and $R_{21} > 1$ for optically thin gas.

We derive a mean $R_{21} > 1$ for our sample which could be interpreted as a source extension smaller than at least the CO(1–0) beam or an extended source and optically thin emission. Based on our data alone, we cannot distinguish between these two cases. We can however consider results for spatially resolved observations from the literature which allows to derive the emission of CO(1–0) and CO(2–1) from the same area so that the source-to-beam size is irrelevant.

Matched aperture observations of CO(1–0) and CO(2–1) give line ratios of $R_{21} = 0.89 \pm 0.6$ (Braine & Combes 1993, for a small sample of nearby spiral galaxies), $R_{21} \sim 0.8$ (Leroy et al. 2009, for the SINGS sample), and $R_{21} \sim 0.6-0.9$ (Casasola et al. 2015, for four low-luminosity AGNs from the NUGA survey). $R_{21} \sim 0.8$ is consistent with optically thick gas with an excitation temperature of ~10 K (Leroy et al. 2009). It is therefore very likely that a similar situation holds in our sample, meaning that $R_{21} > 1$ can be interpreted as optically thick, thermalized gas with a spatial extension smaller than (at least) the CO(1–0) beam.

Based on these assumptions, we can quantify the relation between R_{21} and the source size in a simple model. The relation between the velocity-integrated intensity and the intrinsic source brightness temperature, $T_{\rm B}$, is (Solomon et al. 1997):

$$I_{\rm CO}\Omega_{\rm S*B}(1+z) = T_{\rm B}\triangle V\Omega_{\rm S}, \tag{6}$$

where $\Omega_{\rm S*B}$ is the solid angle of the source convolved with the beam. Adopting for simplicity a source with a Gaussian describes and neglecting the redshift dependence we obtain:

$$I_{\rm CO} = T_{\rm B}\triangle V\frac{\Omega_{\rm S}}{\Omega_{\rm S*B}} = T_{\rm B}\triangle V\frac{\Theta^2_{\rm S}}{\Theta^2_{\rm B}+\Theta^2_{\rm S}}, \tag{7}$$

where Θ_S is the FWHM of the source. With these simplifications, and furthermore assuming that the intrinsic brightness

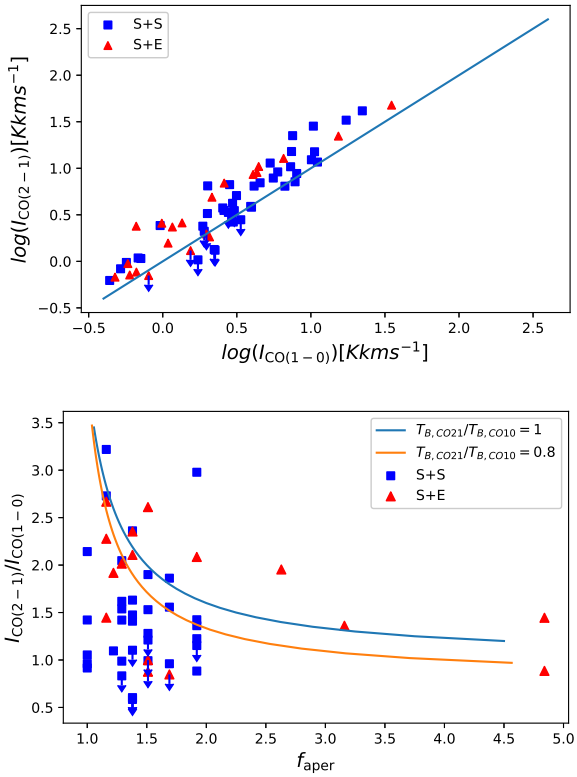

Fig. 2. $I_{CO(2-1)}$ as a function of $I_{CO(1-0)}$ (*top panel*). The line indicates unity. *Lower panel*: line ratio as a function of the aperture correction, f_{aper}, together with the prediction of a simple model assuming a Gaussian source and beam. The model results are shown for two values of the ratio of the intrinsic source brightness temperatures.

temperature T_B is the same for both lines we can describe the line ratio as

$$R_{21} = \frac{I_{CO(2-1)}}{I_{CO(1-0)}} = \frac{\Theta^2_{B(CO10)} + \Theta^2_S}{\Theta^2_{B(CO21)} + \Theta^2_S}. \quad (8)$$

For point-like source ($\Theta^2_S \ll \Theta^2_B$) the line ratio is $R = 4$.

Again adopting Gaussian distributions for both the source and the beam we can derive the aperture correction as a function of beam and source sizes:

$$f_{aper} = \frac{S_{CO,tot}}{S_{CO,center}} = \frac{\Theta^2_S}{\Theta^2_{B(CO10)}} + 1, \quad (9)$$

where $S_{CO,tot}$ is the total flux of the source and $S_{CO,center}$ is the flux observed within the Gaussian CO(1–0) beam. Together, Eqs. (8) and (9) yield a relation between the aperture correction and the line ratio, both derived within the simplifying assumptions made here. We show the resulting relation in Fig. 2. This describes the observed line ratios reasonably well, validating the aperture relation that we use here.

4.3. Molecular gas, atomic gas, and stellar mass

Figure 3 shows the molecular and atomic gas mass of the pairs. There is only a weak correlation (the Spearman's rank correlation coefficient is 0.27 and the significance is 0.096). The ratio between molecular and atomic gas mass is shown in Fig. 4 as a function of stellar mass. The mean molecular-to-atomic gas mass ratio (see Table 4) is significantly higher than the value

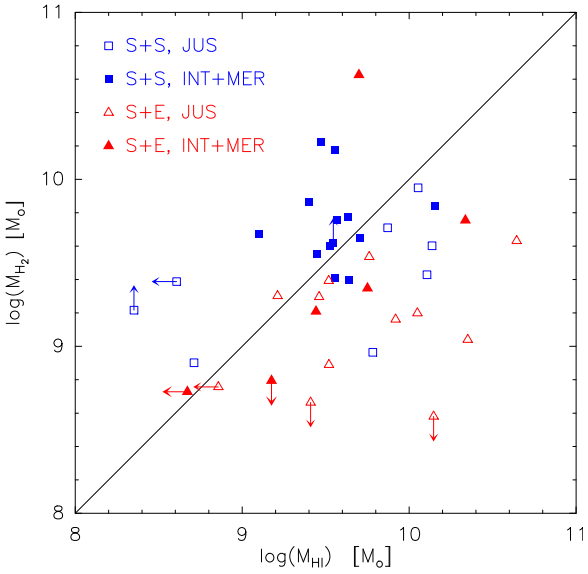

Fig. 3. Molecular gas mass vs. atomic gas mass of galaxy pairs. The values for M_{HI} and M_{H_2} are divided by two for the S+S pair. To guide the eye, we include the line of unity ($M_{HI} = M_{H_2}$, black line).

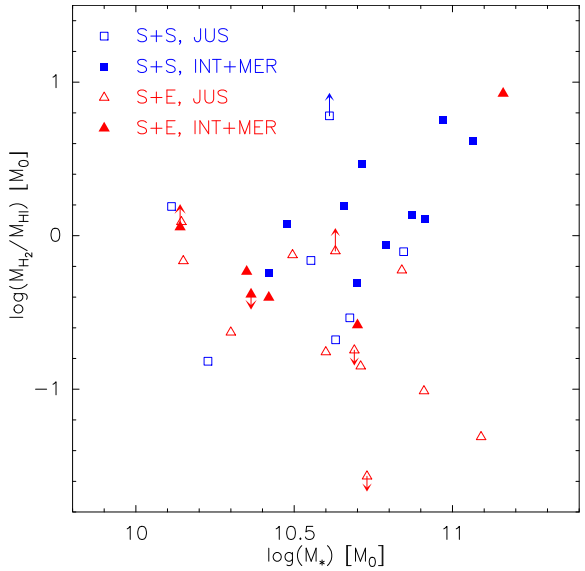

Fig. 4. Ratio between molecular gas mass and atomic gas mass of galaxy pairs as a function of stellar mass. The values for M_{HI} and M_{H_2} are divided by two for the S+S pair.

for the AMIGA comparison sample (by 0.37 ± 0.12 dex). When inspecting the mean values of different subsamples (see Table 4), we find the largest and most significant differences between galaxies with and without morphological signs of interaction. Whereas the JUS sample has a mean $\log(M_{H_2}/M_{HI})$ compatible within the errors with the comparison samples, the INT+MER galaxies have a value which is higher by 0.65 ± 0.16. This difference is more significant for S+S galaxies than for S+E galaxies although the number of galaxies in the corresponding subsamples are very low. There is a difference of 0.55 ± 0.18 dex in $\log(M_{H_2}/M_{HI})$ between S+S and S+E pairs, with the value for a S+E pair being compatible with the comparison sample and that for S+S pairs being higher. As for subsamples with different stellar mass, there is no difference for the entire sample. Only for the subsample of S+S pairs is there a difference

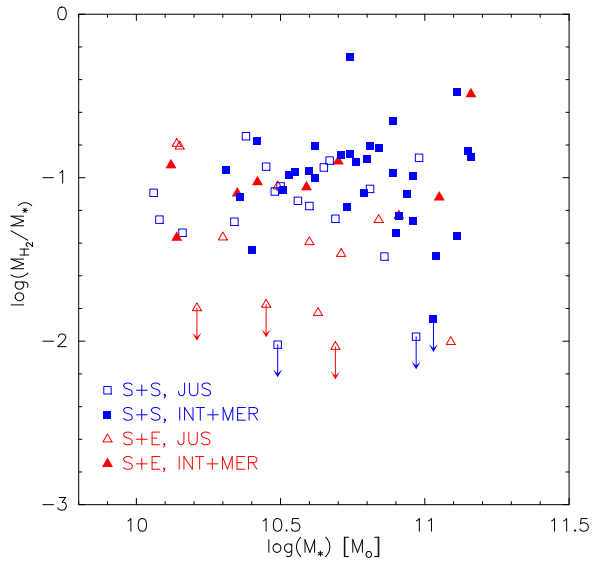

Fig. 5. Molecular gas mass fraction (= M_{H_2}/M_*) vs. stellar mass.

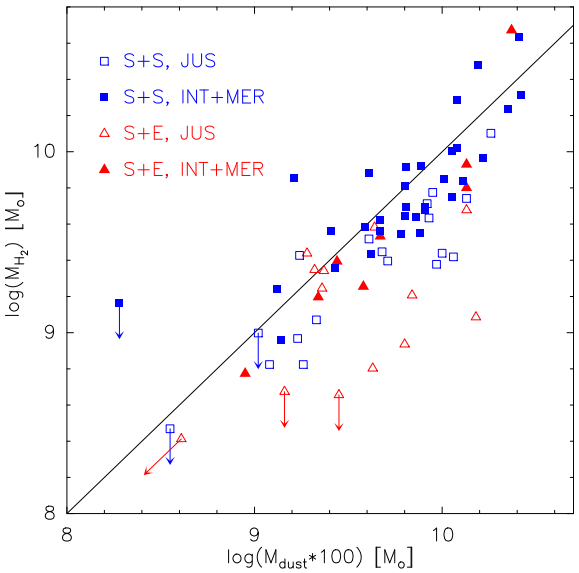

Fig. 7. Molecular gas mass vs. 100× dust mass. The line shows unity.

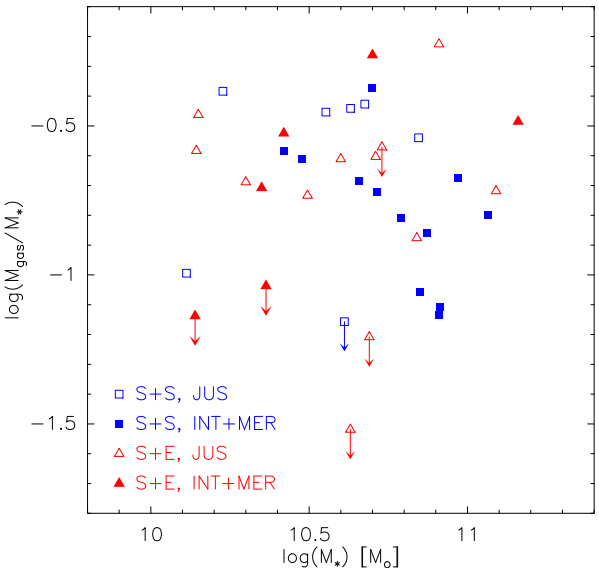

Fig. 6. Total gas mass fraction ($(M_{H_2} + M_{HI})/M_*$) vs. stellar mass of galaxy pairs. The values for M_{dust} and ($M_{HI} + M_{H_2}$) are divided by two for the S+S pair.

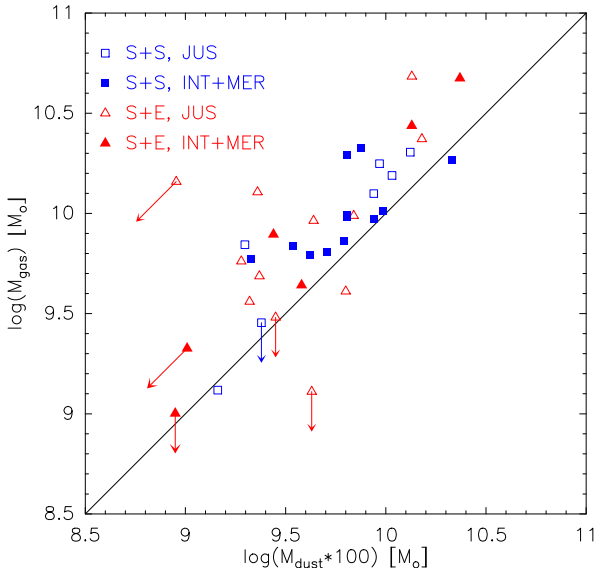

Fig. 8. Total gas (molecular + atomic) mass vs. total 100× dust mass of galaxy pairs. The values for M_{dust} and ($M_{HI} + M_{H_2}$) are divided by two for the S+S pair. The line shows unity.

of 0.51 ± 0.16 dex between low stellar mass ($\log(M_*) < 10.7\ M_\odot$) and high stellar mass ($\log(M_*) > 10.7\ M_\odot$) but the subsamples contain a low number of galaxies.

Figure 5 shows the molecular gas fraction (defined as M_{H_2}/M_*) as a function of stellar mass. The mean logarithmic molecular gas fraction is above the values found for the comparison sample by 0.34 ± 0.07 dex for the AMIGA and by 0.12 ± 0.06 for the COLDGASS sample. Also here, there is a large and significant difference (0.32 ± 0.9 dex) between the mean values of the JUS and INT+MER sample. This difference is also present when considering the S+S and S+E galaxies separately. The molecular gas fraction is also smaller for star-forming galaxies in S+E galaxies compared to S+S galaxies, with a difference of 0.21 ± 0.11 dex (1.9σ). There is no trend with the stellar mass.

The total gas mass fraction ($M_{gas}/M_* = (M_{H_2} + M_{HI})/M_*$) shown in Fig. 6 does not show any trends with stellar mass, pair type (S+S or S+E), or morphological features of interaction.

4.4. Molecular, atomic, and dust mass

Figure 7 demostrates that the molecular gas mass shows a good correlation with the dust mass from Cao et al. (2016). The Spearman's rank correlation coefficient is 0.73 and the significance is 8.4×10^{-12}. The correlation is even tighter with the total gas mass (Fig. 8), with a Spearman's rank correlation coefficient of 0.84 and significance of 3.7×10^{-9}.

Figure 9 shows the ratio between the total gas mass and the dust mass as a function of stellar mass. The mean value is 155 with an error of 12%. No trend with the stellar mass or interaction morphology is visible, nor is there a significant difference between S+S and S+E pairs. The mean value of M_{gas}/M_{dust} for our sample is very close to the mean value for nearby galaxies ($M_{gas}/M_{dust} = 137$; see Table 2 of Draine et al. 2007), with values ranging between approximately 100 and 400. The relatively constant gas-to-dust mass ratio confirms the correctness

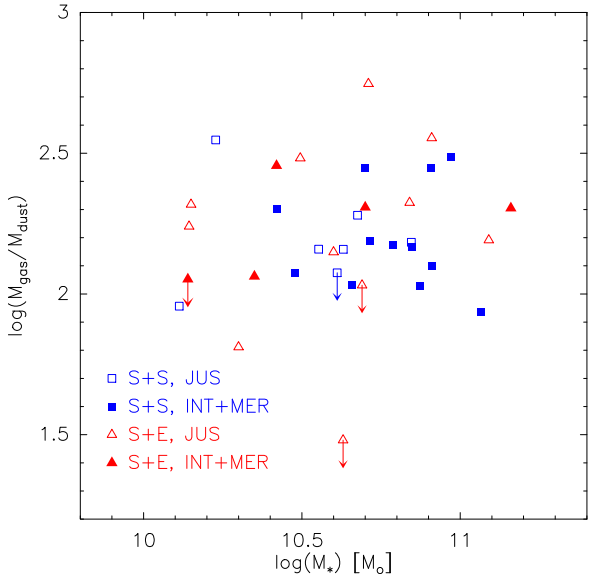

Fig. 9. The gas-to-dust mass ratio vs. stellar mass in galaxy pairs. The values for $M_{\rm dust}$, M_*, and ($M_{\rm HI}$ + $M_{\rm H_2}$) are divided by two for the S+S pair.

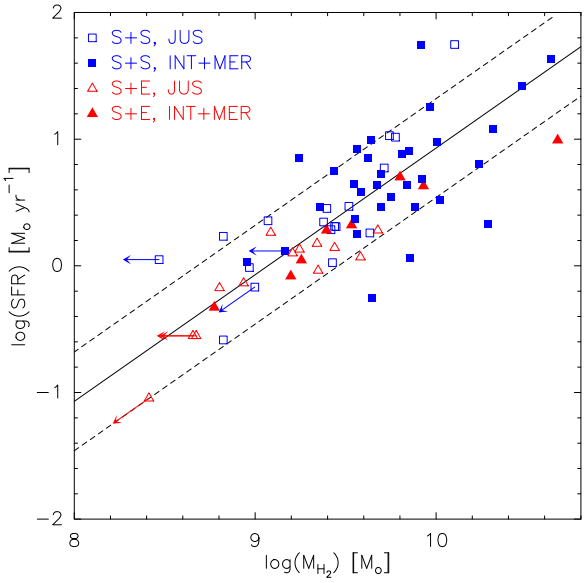

Fig. 10. Star formation rate as a function of molecular gas mass. The lines are not a fit to the data; they show the mean value (full line) and dispersion (dashed lines) of the AMIGA comparison sample.

of the analysis of Cao et al. (2016) who used the dust mass as a gas mass tracer.

4.5. Gas mass, stellar mass, and star formation rate

Figure 10 shows the SFR as a function of $M_{\rm H_2}$. We also show the relation between SFR and $M_{\rm H_2}$ found for the AMIGA sample which is consistent with linearity (Lisenfeld et al. 2011), together with the standard deviation. The galaxies in S+S pairs follow this relation reasonably well, whereas spirals in S+E pairs lie below.

Figure 11 shows the relation between the SFE, defined as the ratio between SFR and molecular gas mass (SFE = SFR/$M_{\rm H_2}$), and the stellar mass. The value of log(SFE) for spirals in S+E pairs is below that of spirals in S+S pairs by 0.18 ± 0.06 dex (see Table 4).

Figure 12 shows the SFR as a function of the total (molecular + atomic) gas mass, and Fig. 13 shows the ratio between SFR and gas mass (SFE$_{\rm gas}$ = SFR/$M_{\rm gas}$). The difference between S+S and S+E spirals is even more pronounced than for the SFE; the value of log(SFE$_{\rm gas}$) is higher by 0.42 ± 0.11 dex for spirals in S+S compared to S+E pairs. Again, no trend with M_* or the interaction phase is found.

This difference in SFE$_{\rm gas}$ between S+S and S+E pairs is in agreement with the results of Cao et al. (2016) who studied the SFE$_{\rm gas}$ using the dust mass as a tracer of the total gas mass for the H-KPAIR sample. They found that log(SFE$_{\rm gas}$) is 0.3 ± 0.1 higher for spirals in S+S pairs than for S+E pairs.

4.6. Holmberg effect

The "Holmberg effect" denotes usually any concordant behaviour between the two components in galaxy pairs, named after the discovery by Holmberg (1937) that binary galaxies tend to have similar morphologies and optical colours. Figure 14 shows the correlation between the molecular gas fraction ($M_{\rm H_2}/M_*$) of the primary and secondary galaxies in S+S pairs. The Spearman's rank correlation coefficient is 0.55 and the significance is 9.4×10^{-3}. A similar Holmberg effect has been found for the sSFR by

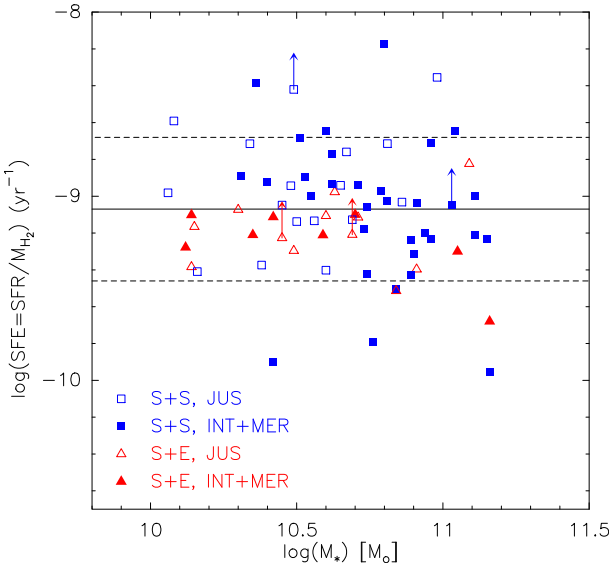

Fig. 11. Star formation efficiency (=(SFR)/$M_{\rm H_2}$) vs. stellar mass. The lines are not a fit to the data; they show the mean value (full line) and dispersion (dashed lines) of the AMIGA comparison sample.

Xu et al. (2010), Cao et al. (2016) and, for a larger sample of 1899 galaxies, by Scudder et al. (2012).

5. Discussion

5.1. Effect of a variable X-factor

We base our analysis on a constant $L'_{\rm CO}$-to-$M_{\rm H_2}$ factor $\alpha_{\rm CO}$. It is well accepted that $\alpha_{\rm CO}$ can vary in different types of galaxies, mainly due to its dependence on metallicity and star formation activity (see Bolatto et al. 2013, and references therein). For example, $\alpha_{\rm CO}$ can be considerably higher for low-metallicity galaxies (below $12 + \log({\rm O/H}) \sim 8.4$, e.g. Leroy et al. 2011; Bolatto et al. 2013; Hunt et al. 2015) and lower by a factor of

Table 4. Mean and median values for different subsamples.

	S+S mean median n/n_{up} [(a)]	S+E mean median n/n_{up} [(a)]	log(M_*)< 10.7 mean median n/n_{up} [(a)]	log(M_*)> 10.7 mean median n/n_{up} [(a)]	JUS mean median n/n_{up} [(a)]	INT+MER mean median n/n_{up} [(a)]	Total mean median n/n_{up} [(a)]
log(SFE)	**−9.02 ± 0.05** −9.00 49/2	**−9.20 ± 0.04** −9.17 20/2	−9.02 ± 0.05 −9.05 38/3	−9.13 ± 0.07 −9.18 31/1	−9.02 ± 0.06 −9.07 29/3	−9.10 ± 0.06 −9.10 40/1	−9.07 ± 0.04 −9.10 69/4
log(SFE) S+S	–	–	−8.96 ± 0.07 −8.94 24/1	−9.09 ± 0.08 −9.06 25/1	−8.94 ± 0.08 −8.98 17/1	−9.07 ± 0.07 −9.03 32/1	–
log(SFE) S+E	–	–	−9.16 ± 0.03 −9.11 14/2	−9.30 ± 0.11 −9.30 6/0	−9.16 ± 0.06 −9.11 12/2	−9.25 ± 0.06 −9.21 8/0	–
log(SFE_{gas})	**−9.31 ± 0.08** −9.33 19/1	**−9.73 ± 0.07** −9.68 16/3	−9.46 ± 0.06 −9.50 20/4	−9.52 ± 0.13 −9.61 15/0	−9.59 ± 0.10 −9.60 18/3	−9.36 ± 0.09 −9.45 17/1	−9.48 ± 0.07 −9.50 35/4
log(SFE_{gas}) S+S	–	–	−9.40 ± 0.07 −9.42 10/1	−9.23 ± 0.13 −9.22 9/0	−9.36 ± 0.12 −9.33 7/1	−9.28 ± 0.10 −9.33 12/0	– –
log(SFE_{gas}) S+E	–	–	**−9.57 ± 0.06** −9.60 10/3	**−9.97 ± 0.10** −9.90 6/0	−9.80 ± 0.09 −9.75 11/2	−9.59 ± 0.06 −9.61 5/1	– –
log(M_{H_2}/M_{HI})	**0.00 ± 0.10** 0.07 18/0	**−0.55 ± 0.15** −0.58 16/3	−0.33 ± 0.08 −0.31 18/2	−0.14 ± 0.18 −0.06 16/1	**−0.57 ± 0.12** −0.63 17/2	**0.08 ± 0.11** 0.07 17/1	−0.26 ± 0.10 −0.16 34/3
log(M_{H_2}/M_{HI}) S+S			**−0.25 ± 0.12** −0.24 9/0	**0.26 ± 0.11** 0.14 9/0	**−0.35 ± 0.15** −0.16 6/0	**0.18 ± 0.10** 0.11 12/0	–
log(M_{H_2}/M_{HI}) S+E			−0.40 ± 0.10 −0.40 9/2	−0.66 ± 0.29 −0.85 7/1	−0.70 ± 0.16 −0.76 11/2	−0.15 ± 0.25 −0.40 5/1	–
log(M_{H_2}/M_*)	−1.08 ± 0.05 −1.00 50/3	−1.29 ± 0.10 −1.23 21/3	−1.18 ± 0.06 −1.05 39/4	−1.10 ± 0.07 −1.06 32/2	**−1.32 ± 0.07** −1.23 31/5	**−1.00 ± 0.05** −0.97 40/31	−1.14 ± 0.05 −1.08 71/6
log(M_{H_2}/M_*) S+S		–	−1.10 ± 0.05 −1.05 24/1	−1.06 ± 0.08 −0.97 26/2	**−1.20 ± 0.08** −1.14 18/2	**−1.00 ± 0.05** −0.97 32/1	
log(M_{H_2}/M_*) S+E			−1.30 ± 0.11 −1.10 15/3	−1.26 ± 0.18 −1.23 6/0	**−1.47 ± 0.12** −1.39 13/3	**−1.00 ± 0.08** −1.03 8/0	
log(M_{gas}/M_*)	−0.73 ± 0.06 −0.69 19/1	−0.81 ± 0.10 −0.69 18/5	−0.80 ± 0.09 −0.61 21/5	−0.73 ± 0.07 −0.72 16/1	−0.75 ± 0.09 −0.61 19/4	−0.76 ± 0.06 −0.72 18/2	−0.77 ± 0.06 −0.69 37/6
log(M_{gas}/M_{dust})	2.19±0.04 2.17 19/1	2.17±0.09 2.30 16/3	2.12±0.07 2.15 20/4	2.28±0.05 2.19 15/0	2.17±0.08 2.18 18/3	2.21±0.04 2.17 17/1	2.19±0.05 2.18 35/4

Notes. Mean values for which the difference between the complementary subsamples of $\gtrsim 2\sigma$ is printed in boldface. [(a)]Total number of galaxies (n) and number of upper limits (n_{up}).

3–10 in extreme starbursts, as in ULIRGS (Downes & Solomon 1998, 2003).

Our sample does not contain low-metallicity galaxies because all galaxies have relatively high masses ($>10^{10}$ $M_\odot$), and neither does it contain extreme starburst galaxies, meaning that we do not expect α_{CO} to vary considerably among them. We can test whether we find any indications of a relation with the SF activity by comparing the gas-to-dust mass ratio to the sSFR (Fig. 15). If the molecular gas mass is correctly calculated we expect no trend with the sSFR. If on the other hand α_{CO} were found to decrease with the SF activity we would expect to see an overestimation of M_{H_2} and thus an increase of the gas-to-dust mass ratio for increasing sSFR. This is not the case, even for those objects where the molecular gas is dominating the gas mass. At most, there might be a weak trend in the opposite direction (decreasing gas mass with sSFR).

In spite of this lack of evidence for a variation of α_{CO} in our sample, we test the effect of a possible variation loosely following the prescription proposed in Violino et al. (2018) and Sargent et al. (2014) who parametrized the variation of the

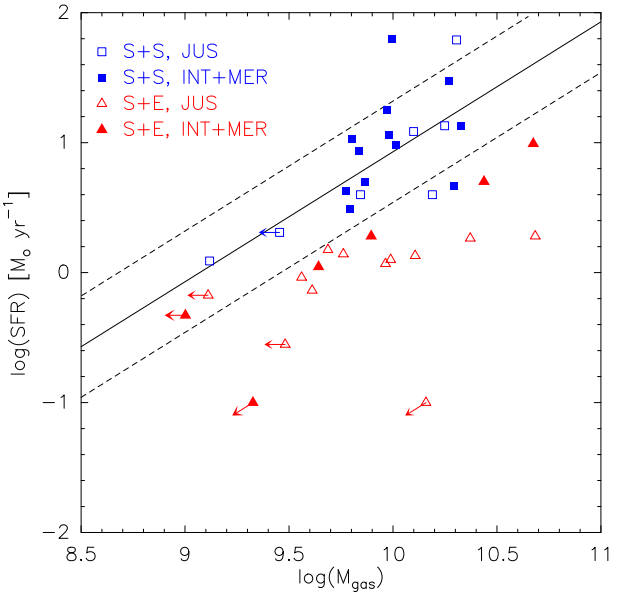

Fig. 12. Star formation rate as a function of total (molecular+atomic) gas mass. To guide the eye, the lines are the same as in Fig. 10 and show the mean value (full line) and dispersion (dashed lines) of the AMIGA comparison sample.

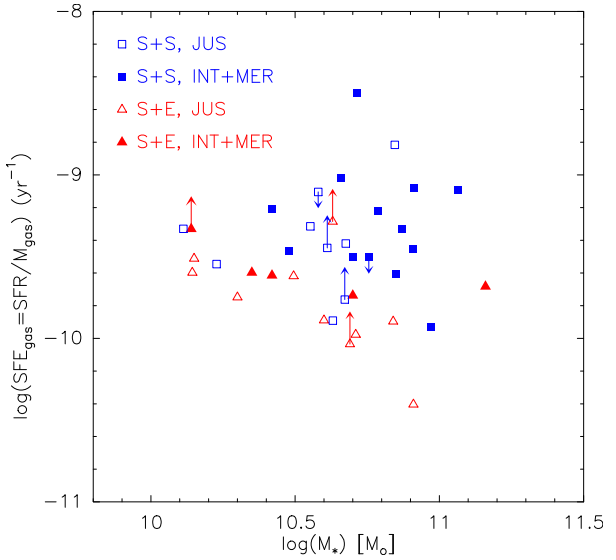

Fig. 13. Star formation efficiency per total gas mass ($\mathrm{SFE_{gas}} = (\mathrm{SFR})/M_{\mathrm{gas}}$) vs. stellar mass.

conversion factor as:

$$\alpha_{\mathrm{CO}} = (1 - f_{\mathrm{SB}})\alpha_{\mathrm{CO,MS}} + f_{\mathrm{SB}}\alpha_{\mathrm{SB}}, \quad (10)$$

where $\alpha_{\mathrm{CO,MS}}$ is the conversion factor for galaxies lying on the galaxy main sequence, $\alpha_{\mathrm{CO,SB}}$ is the value for extreme starburst galaxies, and f_{SB} is the probability of a galaxy being in a starburst phase given its offset from the mean locus of the star-forming main sequence in the SFR-M_* plane. Violino et al. (2018) take into account a metallicity dependence of $\alpha_{\mathrm{CO,MS}}$, which we do not consider necessary for our high-mass sample, meaning that we take $\alpha_{\mathrm{CO,MS}}$ as the Galactic X-factor from Bolatto et al. (2013), $\alpha_{\mathrm{CO,MS}} = 3.2\,M_\odot/(\mathrm{K\,km\,s^{-1}\,pc^{-2}})$. We assume that f_{SB} varies linearly with the logarithmic distance of a galaxy from the galaxy main sequence, $\Delta_{\mathrm{MS}} = \log(\mathrm{SFR}) - \log(\mathrm{SFR_{MS}})$. We use the MS location following the prescription by Saintonge et al. (2016, their Eq. (5)) because their sample encompasses roughly the same mass range as ours. We normalize f_{SB} by taking Arp 220 as a prototypical extreme starburst galaxy. Deriving the stellar mass from the K-band luminosity and the SFR from the far-infrared luminosity, we obtain $M_* = 1.4 \times 10^{10}\,M_\odot$ and SFR $= 220\,M_\odot\,\mathrm{yr^{-1}}$ and find that Arp 220 lies a factor of 100 above the main sequence. We adopt $\alpha_{\mathrm{CO,SB}} = 0.8\,M_\odot/(\mathrm{K\,km\,s^{-1}\,pc^{-2}})$ from Downes & Solomon (1998). Together, this yields, for a linear relation between f_{SB} and Δ_{MS}, $f_{\mathrm{SB}} = \Delta_{\mathrm{MS}}/\log(100) = \Delta_{\mathrm{MS}}/2$. Finally, we assume that galaxies that fall below the MS have the Galactic α_{CO} (i.e. $f_{\mathrm{SB}} = 0$).

We test all our results with this different prescription. The results obtained with this variable α_{CO} are very similar to the ones with a constant Galactic value. The differences are within the errors, and in particular all the differences and correlations that we found are also valid for a variable α_{CO}. Therefore we conclude that our results are robust with respect to reasonable uncertainties in the X-factor.

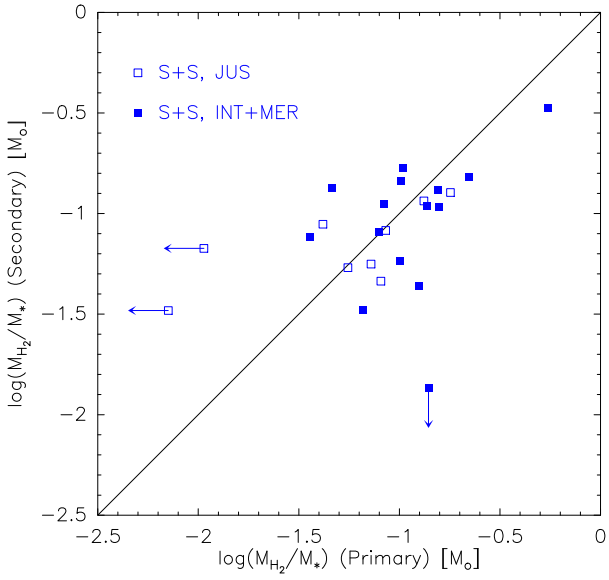

Fig. 14. Molecular gas fraction of the secondary vs. primary galaxy in S+S pairs.

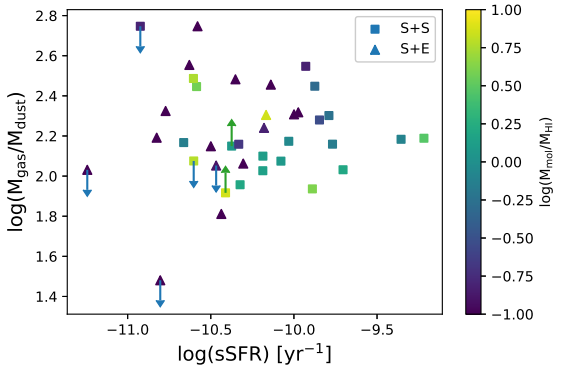

Fig. 15. Gas-to-dust mass ratio as a function of the sSFR.

5.2. Variations of the star formation efficiency

Compared to the AMIGA sample (Table 3), we find no enhancement in the SFE for the whole pair sample, or for any of the subsamples (S+S and S+E, low mass and high mass, with and without interaction signs; see Table 4). Whether or not paired galaxies

have enhanced SFE compared to normal spirals is debated in the literature. While Violino et al. (2018) and Pan et al. (2018) found weakly enhanced SFE ($\lesssim$2×), whereas Solomon & Sage (1988), Combes et al. (1994), and Casasola et al. (2004) found no such enhancement.

We found a $\sim 3\sigma$ difference of (0.18 ± 0.06 dex) between the SFE of galaxies in S+S and in S+E pairs. Compared to the AMIGA sample, the SFE in S+E is slightly decreased by 0.13 ± 0.06 dex, indicating a lower capacity of the molecular gas to form stars in S+E pairs. The difference with respect to the comparison sample is small and might be affected by systematic uncertainties, for example those stemming from differences in the calculation of the SFR. The difference between the S+S and S+E subsample is more robust; it holds at a 3σ level when using a variable α_{CO} (0.25±0.08 dex) and when considering the central values for the molecular gas and SFR (0.22±0.06 dex). The physical reason for this difference is unclear. A possible reason could be hydrodynamical effects which are expected to be stronger in a S+S merger where the gas of both galaxies interacts compared to S+E mergers where the elliptical component has very little cold gas. However, we would then expect to see a noticeable difference mainly in the later stages of the interaction, whereas in our study we find no differences in the SFE between galaxies with and without signs of interaction. Hwang et al. (2011) suggested that the hot-gas halos around elliptical galaxies could be responsible for the differences in the SF activity found between S+S and S+E. However, it is unclear how the hot gas can directly affect the molecular gas without altering the total (M_{HI} + M_{H_2}) gas content which we found to be the same for all subsamples.

When considering the total gas, our results show significant enhancement in SFE_{gas} for S+S pairs (0.42 ± 0.09 dex), pairs with signs of interaction (0.37 ± 0.10 dex), and low-mass pairs (0.27±0.08 dex), but not for subsamples of S+E pairs, pairs without signs of interaction, and high-mass pairs. Simulations (e.g. Renaud et al. 2014) have predicted enhanced SFE_{gas} in interacting galaxies, which is particularly strong during the final stage of a merger, but also during the early phase just after the first pericentre passage. Our results suggest that this scenario applies to S+S pairs, but not to S+E pairs. The mean SFE_{gas} of the S+E subsample is consistent with that of control galaxies, and is lower than that of the S+S subsample by 0.42 ± 0.11 dex. This result agrees well with that of Cao et al. (2016) who found a difference between the mean SFE_{gas} of S+S and S+E pairs of 0.43 ± 0.13 dex.

5.3. Variation of the molecular gas fraction

The molecular gas fraction (M_{H_2}/M_*) and molecular-to-atomic gas ratio (M_{H_2}/M_{HI}) are enhanced for INT+MER galaxies whereas for pairs at the beginning of the interaction (JUS) no enhancement is found. Significant enhancement is also present in S+S pairs but not in S+E pairs. The total gas content (M_{gas}/M_*) on the other hand does not show any variation between the subsamples.

These results together give a consistent picture. From the total gas content in the galaxy, a considerable fraction is converted from atomic to molecular gas during the interaction. This conversion becomes stronger in a later stage, when morphological signatures are visible. We would then expect a similar trend for the sSFR caused by the increase in the molecular gas fraction. Indeed, Cao et al. (2016) found a higher sSFR for INT+MER galaxies compared to JUS galaxies.

Our results are in general consistent with numerous previous observations that showed significant increase in the molecular gas content in interacting galaxies (Braine & Combes 1993; Combes et al. 1994; Casasola et al. 2004; Violino et al. 2018; Pan et al. 2018). Our results however indicate that not all galaxies in close major-merger pairs have an enhanced molecular gas content, but only those in S+S pairs and pairs with interaction signs.

With a statistically significant, large, and homogeneous sample of paired galaxies confined to close major-merger pairs that have small separations and mass ratios, we pinpoint that the major enhancement occurs in the molecular-to-atomic gas ratio. This conclusion disagrees with Casasola et al. (2004). They investigated the molecular-to-atomic gas ratios of interacting galaxies and found that for late types these ratios are quite normal compared to the control sample. Given that both the interacting galaxy sample and the control sample of Casasola et al. (2004) were constructed heterogeneously, together with the multi-band data collected from the literature, their result most likely has larger uncertainties than ours, and most importantly their data does not allow a distinction between pair type and interaction phase, which we found to be crucial in finding a difference in M_{H_2}/M_{HI}.

5.4. What drives the enhancement of the SFR in galaxy pairs?

Our results show that the increase of the SFR in close major-merger pairs is mainly driven by an enhancement in the molecular-to-HI gas ratio. The total gas content on the other hand is constant, meaning that inflow or loss of gas can be excluded. The SFE is not significantly enhanced compared to control galaxies, while the increase in the SFE_{gas} can be explained by the enhancement of the molecular-to-HI gas ratio. Given that the enhancement is found only in pairs with signs of interaction and is absent in pairs without, it is most likely triggered by the strong tidal torque after the first close encounter, which can compress the lower-density HI gas into the higher-density molecular gas. This scenario is different from that for (U)LIRGs which are in the final stage of coalescence. For (U)LIRGs, both the molecular gas content and SFE are strongly enhanced (Solomon & Sage 1988; Mirabel & Sanders 1989). It seems that in paired galaxies after the first close encounter, while the tidal torque compresses more gas into star-forming giant molecular clouds (GMCs), the SFE of individual GMCs is still comparable to the standard value found in normal galaxies (Leroy et al. 2008). On the other hand, in (U)LIRGs such as Arp220, the GMCs in the central starburst are further compressed into a gas disk of very high density ($>10^4$ cm^{-3}), resulting in a much higher SFE (Scoville et al. 1997, 2017). Gao & Solomon (1999) found that, for infrared-selected mergers, the L_{IR}/M_{H_2} ratio increases by nearly ten times when projected separation decreases from ∼30 to ∼2 kpc, consistent with a continuous transition of the SFE between close pairs and final-stage mergers.

This change of SFE of molecular gas along the merger sequence may provide a new and important constraint to simulations of galaxy mergers. Currently, no simulation has separated molecular gas from atomic gas. An indirect inference may be drawn from the results of Renaud et al. (2014), who carried out parsec-resolution simulations with comprehensive treatment of turbulence and shocks. In their Fig. 2, they presented predictions of gas-density probability distribution functions (PDFs) of different merger epochs, with the t = 35 Myr epoch corresponding to the starburst after the first close encounter and the t = 170 Myr epoch to the starburst in the final coalescence. For both epochs, strong enhancements are found both in the ratio between densities of ∼100 cm^{-3} and ∼1 cm^{-3}, which corresponds roughly to the molecular-to-atomic gas ratio, and in

the ratio between densities of $\sim 10^4\,\mathrm{cm}^{-3}$ and $\sim 100\,\mathrm{cm}^{-3}$. The mass of dense gas of $\sim 10^4\,\mathrm{cm}^{-3}$ is linearly correlated to SFR (Gao & Solomon 2004), therefore the enhancement in the ratio between densities of $\sim 10^4\,\mathrm{cm}^{-3}$ and $\sim 100\,\mathrm{cm}^{-3}$ indicates an SFE enhancement both in the epoch after the first close encounter and in the final coalescence stage. This seems not fully consistent with our result which does not show strong SFE enhancement in paired galaxies.

We found differences in the SFE, $\mathrm{SFE_{gas}}$, and $M_{\mathrm{H_2}}/M_{\mathrm{HI}}$ between S+S and S+E subsamples. In particular, the mean $M_{\mathrm{H_2}}/M_{\mathrm{HI}}$ ratio of the S+E is 0.55 ± 0.18 dex lower than that of S+S (Table 4), and is consistent with those of the control samples (Table 3). The difference is caused by two factors: (1) only 31% (5/16) of star-forming galaxies in S+E show signs of interaction while 67% (12/18) of those in S+S do; and (2) the mean $M_{\mathrm{H_2}}/M_{\mathrm{HI}}$ ratio of star-forming galaxies in S+E pairs without signs of interaction is 0.35 ± 0.22 dex lower than that of their counterparts in S+S. The first factor might be explained by the stabilising effect that bulges can have during interaction, if star-forming galaxies in S+E are more likely to be earlier Hubble types with larger bulges compared to their counterparts in S+S, which is indeed expected according to the Holmberg effect (Holmberg 1958; Hernández-Toledo & Puerari 2001). Simulations have shown that large bulges can suppress the tidal effects during and after close encounters (Mihos & Hernquist 1996; Di Matteo et al. 2008; Cox et al. 2008), making it more difficult for conspicuous tidal features to form. Interestingly, star-forming galaxies in S+E pairs with interaction signs show an enhancement of 0.55 ± 0.30 dex in $M_{\mathrm{H_2}}/M_{\mathrm{HI}}$ ratio compared to those in S+E pairs without interaction signs, suggesting that HI gas can also be compressed to molecular gas in S+E pairs when the tidal effects are sufficiently strong (indicated by interaction signs), similar to what is happening in S+S pairs with interaction signs. The factor (2), though with a low significance (1.6σ), might indicate that the progenitors of star-forming galaxies in S+E have lower $M_{\mathrm{H_2}}/M_{\mathrm{HI}}$ than those in S+S. Alternatively, the formation of the molecular gas due to tidal forces might have started early in the interaction and preferentially in the bulgeless S+S systems.

6. Conclusions and summary

We presented new CO data for a sample of K_s-band-selected local ($z < 0.06$), close (projected separation $\lesssim 20\,h^{-1}$ kpc), and major (mass ratio ≤ 2.5) merger pairs which allow us to calculate the molecular gas mass. These data, together with a large set of ancillary data, allow us to study the molecular gas fraction, $M_{\mathrm{H_2}}/M_*$, the molecular-to-atomic gas mass ratio, $M_{\mathrm{H_2}}/M_{\mathrm{HI}}$, $\mathrm{SFE} = \mathrm{SFR}/M_{\mathrm{H_2}}$, and $\mathrm{SFE_{gas}} = \mathrm{SFR}/M_{\mathrm{gas}}$ as a function of galaxy mass, interaction type (S+S or S+E pair) and interaction phase (undisturbed appearance "JUS", or with clear signs of tidal disturbance or merging "INT+MER"). We compared the values of the merger sample to two comparison samples, AMIGA (Lisenfeld et al. 2011) and COLDGASS (Saintonge et al. 2011a,b). The main conclusions are:

1. We found no significant enhancement in SFE ($= \mathrm{SFR}/M_{\mathrm{H_2}}$) for the whole pair sample, nor for any of the subsamples (S+S and S+E, low mass and high mass, or with and without signs of interaction). The SFE in star-forming galaxies in S+E pairs is 0.18 ± 0.06 dex lower than in S+S pairs.
2. When considering the total gas, $M_{\mathrm{gas}} = M_{\mathrm{HI}} + M_{\mathrm{H_2}}$, our results show significant enhancement in $\mathrm{SFE_{gas}}$ for S+S pairs (0.42 ± 0.09 dex), pairs with signs of interaction (0.37 ± 0.10 dex), and low-mass pairs (0.27 ± 0.08 dex), but not for subsamples of S+E pairs, pairs without signs of interaction, and high-mass pairs.
3. We found an enhancement of $M_{\mathrm{H_2}}/M_{\mathrm{HI}}$ from JUS to INT+MER galaxies. The values of the JUS subsample are compatible with those of the control samples. A similar, albeit less significant trend was found for $M_{\mathrm{H_2}}/M_*$. This indicates that the amount of molecular gas enhances as the interaction proceeds.
4. We found differences in $M_{\mathrm{H_2}}/M_{\mathrm{HI}}$ and in $M_{\mathrm{H_2}}/M_*$ between S+S and S+E subsamples. The mean $M_{\mathrm{H_2}}/M_{\mathrm{HI}}$ ratio and mean $M_{\mathrm{H_2}}/M_*$ ratio of the S+E are 0.55 ± 0.18 dex (3σ) and 0.21 ± 0.11 dex (1.9σ) lower than those of the S+S, respectively, and are consistent with those of control samples.

Our results show that the star formation enhancement in close major-merger pairs is mainly driven by an accelerated conversion of atomic gas to molecular gas in pairs with interaction signs, likely triggered by the strong tidal effects after the first close encounter. Both the star formation and molecular gas content enhancements are significantly suppressed in star-forming galaxies in S+E pairs, probably due to the stabilising effects of large bulges.

Acknowledgements. CKX acknowledges support from the National Key R&D Program of China No. 2017YFA0402704 and National Natural Science Foundation of China No. Y811251N01. UL acknowledge support by the research projects AYA2014-53506-P and AYA2017-84897-P from the Spanish Ministerio de Economía y Competitividad, from the European Regional Development Funds (FEDER) and the Junta de Andalucía (Spain) grants FQM108. YG acknowledges the NSFC grants#11420101002 and 11861131007, the National Key R&D Program of China grant #2017YFA0402700, and the CAS Key Frontier Sciences Program. PZ acknowledges support from the National Science Foundation of China (grant No. 11721303) and the National Key R&D Program of China (grant No. 2016YFA0400702). This work is sponsored in part by the Chinese Academy of Sciences (CAS), through a grant to the CAS South America Center for Astronomy (CASSACA) in Santiago, Chile. This work is based on observations carried out under project numbers 071-12 and 177-15 with the IRAM 30 m telescope. IRAM is supported by INSU/CNRS (France), MPG (Germany) and IGN (Spain).

References

Argudo-Fernández, M., Verley, S., Bergond, G., et al. 2015, A&A, 578, A110
Barnes, J. E., & Hernquist, L. 1992, ARA&A, 30, 705
Bell, E. F., & de Jong, R. S. 2001, ApJ, 550, 212
Bettoni, D., Galletta, G., & García-Burillo, S. 2003, A&A, 405, 5
Bolatto, A. D., Wolfire, M., & Leroy, A. K. 2013, ARA&A, 51, 207
Boselli, A., Cortese, L., & Boquien, M. 2014, A&A, 564, A65
Braine, J., & Combes, F. 1993, A&A, 269, 7
Buat, V., & Xu, C. 1996, A&A, 306, 61
Buat, V., Giovannoli, E., Takeuchi, T. T., et al. 2011, A&A, 529, A22
Cao, C., Xu, C. K., Domingue, D., et al. 2016, ApJS, 222, 16
Casasola, V., Bettoni, D., & Galletta, G. 2004, A&A, 422, 941
Casasola, V., Hunt, L., Combes, F., & García-Burillo, S. 2015, A&A, 577, A135
Casasola, V., Cassarà, L. P., Bianchi, S., et al. 2017, A&A, 605, A18
Catinella, B., Saintonge, A., Janowiecki, S., et al. 2018, MNRAS, 476, 875
Combes, F., Prugniel, P., Rampazzo, R., & Sulentic, J. W. 1994, A&A, 281, 725
Corbelli, E., Bianchi, S., Cortese, L., et al. 2012, A&A, 542, A32
Cox, T. J., Jonsson, P., Somerville, R. S., Primack, J. R., & Dekel, A. 2008, MNRAS, 384, 386
Di Matteo, P., Combes, F., Melchior, A.-L., & Semelin, B. 2007, A&A, 468, 61
Di Matteo, P., Bournaud, F., Martig, M., et al. 2008, A&A, 492, 31
Domingue, D. L., Xu, C. K., Jarrett, T. H., & Cheng, Y. 2009, ApJ, 695, 1559
Domingue, D. L., Cao, C., Xu, C. K., et al. 2016, ApJ, 829, 78
Downes, D., & Solomon, P. M. 1998, ApJ, 507, 615
Downes, D., & Solomon, P. M. 2003, ApJ, 582, 37
Draine, B. T., Dale, D. A., Bendo, G., et al. 2007, ApJ, 663, 866
Dressler, A. 1980, ApJ, 236, 351
Duplancic, F., Alonso, S., Lambas, D. G., & O'Mill, A. L. 2015, MNRAS, 447, 1399
Eales, S., Smith, M. W. L., Auld, R., et al. 2012, ApJ, 761, 168
Ellison, S. L., Patton, D. R., Simard, L., et al. 2010, MNRAS, 407, 1514

Ellison, S. L., Mendel, J. T., Scudder, J. M., Patton, D. R., & Palmer, M. J. D. 2013, MNRAS, 430, 3128
Gao, Y., & Solomon, P. M. 1999, ApJ, 512, L99
Gao, Y., & Solomon, P. M. 2004, ApJ, 606, 271
Hernández-Toledo, H. M., & Puerari, I. 2001, A&A, 379, 54
Hickson, P., de Mens Oliveira, C., Huchra, J.P., & Palumbo, G.G. 1992, ApJ, *399*, 353
Holmberg, E. 1937, Ann. Obs. Lund, 6, 1
Holmberg, E. 1958, Lund Medd. Astron. Obs. Ser. II, 136, 1
Hunt, L. K., García-Burillo, S., Casasola, V., et al. 2015, A&A, 583, A114
Hwang, H. S., Elbaz, D., Dickinson, M., et al. 2011, A&A, 535, A60
Kauffmann, G., Li, C., Zhang, W., & Weinmann, S. 2013, MNRAS, 430, 1447
Kennicutt, Jr., R. C. 1998, ARA&A, 36, 189
Kennicutt, Jr., R. C., Keel, W. C., van der Hulst, J. M., Hummel, E., & Roettiger, K. A. 1987, AJ, 93, 1011
Kuno, N., Sato, N., Nakanishi, H., et al. 2007, PASJ, 59, 117
Lam, M. I., Wu, H., Zhu, Y.-N., & Zhou, Z.-M. 2013, Res. Astron. Astrophys., 13, 179
Leroy, A. K., Walter, F., Brinks, E., et al. 2008, AJ, 136, 2782
Leroy, A. K., Walter, F., Bigiel, F., et al. 2009, AJ, 137, 4670
Leroy, A. K., Bolatto, A., Gordon, K., et al. 2011, ApJ, 737, 12
Lisenfeld, U., Verdes-Montenegro, L., Sulentic, J., et al. 2007, A&A, 462, 507
Lisenfeld, U., Espada, D., Verdes-Montenegro, L., et al. 2011, A&A, 534, A102
Lisenfeld, U., Alatalo, K., Zucker, C., et al. 2017, A&A, 607, A110
Mihos, J. C., & Hernquist, L. 1996, ApJ, 464, 641
Mirabel, I. F., & Sanders, D. B. 1989, ApJ, 340, L53
Moore, B., Katz, N., Lake, G., Dressler, A., & Oemler, A. 1996, Nature, 379, 613
Nikolic, B., Cullen, H., & Alexander, P. 2004, MNRAS, 355, 874
Nishiyama, K., Nakai, N., & Kuno, N. 2001, PASJ, 53, 757
Nordon, R., Lutz, D., Genzel, R., et al. 2012, ApJ, 745, 182
Pan, H.-A., Lin, L., Hsieh, B.-C., et al. 2018, ApJ, 868, 132
Regan, M. W., Thornley, M. D., Helfer, T. T., et al. 2001, ApJ, 561, 218
Renaud, F., Bournaud, F., Kraljic, K., & Duc, P.-A. 2014, MNRAS, 442, L33
Saintonge, A., Kauffmann, G., Kramer, C., et al. 2011a, MNRAS, 415, 32
Saintonge, A., Kauffmann, G., Wang, J., et al. 2011b, MNRAS, 415, 61
Saintonge, A., Catinella, B., Cortese, L., et al. 2016, MNRAS, 462, 1749
Sanders, D. B., & Mirabel, I. F. 1996, ARA&A, 34, 749
Sargent, M. T., Daddi, E., Béthermin, M., et al. 2014, ApJ, 793, 19
Scoville, N. Z., Yun, M. S., & Bryant, P. M. 1997, ApJ, 484, 702
Scoville, N., Murchikova, L., Walter, F., et al. 2017, ApJ, 836, 66
Scudder, J. M., Ellison, S. L., Torrey, P., Patton, D. R., & Mendel, J. T. 2012, MNRAS, 426, 549
Sofue, Y., Wakamatsu, K.-I., Taniguchi, Y., & Nakai, N. 1993, PASJ, 45, 43
Solomon, P. M., & Sage, L. J. 1988, ApJ, 334, 613
Solomon, P. M., Downes, D., Radford, S. J. E., & Barrett, J. W. 1997, ApJ, 478, 144
Teyssier, R., Chapon, D., & Bournaud, F. 2010, ApJ, 720, L149
Verdes-Montenegro, L., Sulentic, J., Lisenfeld, U., et al. 2005, A&A, 436, 443
Violino, G., Ellison, S. L., Sargent, M., et al. 2018, MNRAS, 476, 2591
Xu, C., & Sulentic, J. W. 1990, in NASA Conf. Publ., eds. J. W. Sulentic, W. C. Keel, & C. M. Telesco, 3098
Xu, C. K., Domingue, D., Cheng, Y.-W., et al. 2010, ApJ, 713, 330
Xu, C. K., Zhao, Y., Scoville, N., et al. 2012, ApJ, 747, 85
Yamauchi, C., Ichikawa, S.-I., Doi, M., et al. 2005, AJ, 130, 1545
Yuan, F.-T., Takeuchi, T. T., Matsuoka, Y., et al. 2012, A&A, 548, A117
Zuo, P., Xu, C. K., Yun, M. S., et al. 2018, ApJS, 237, 2

Appendix A: Figures of spectra

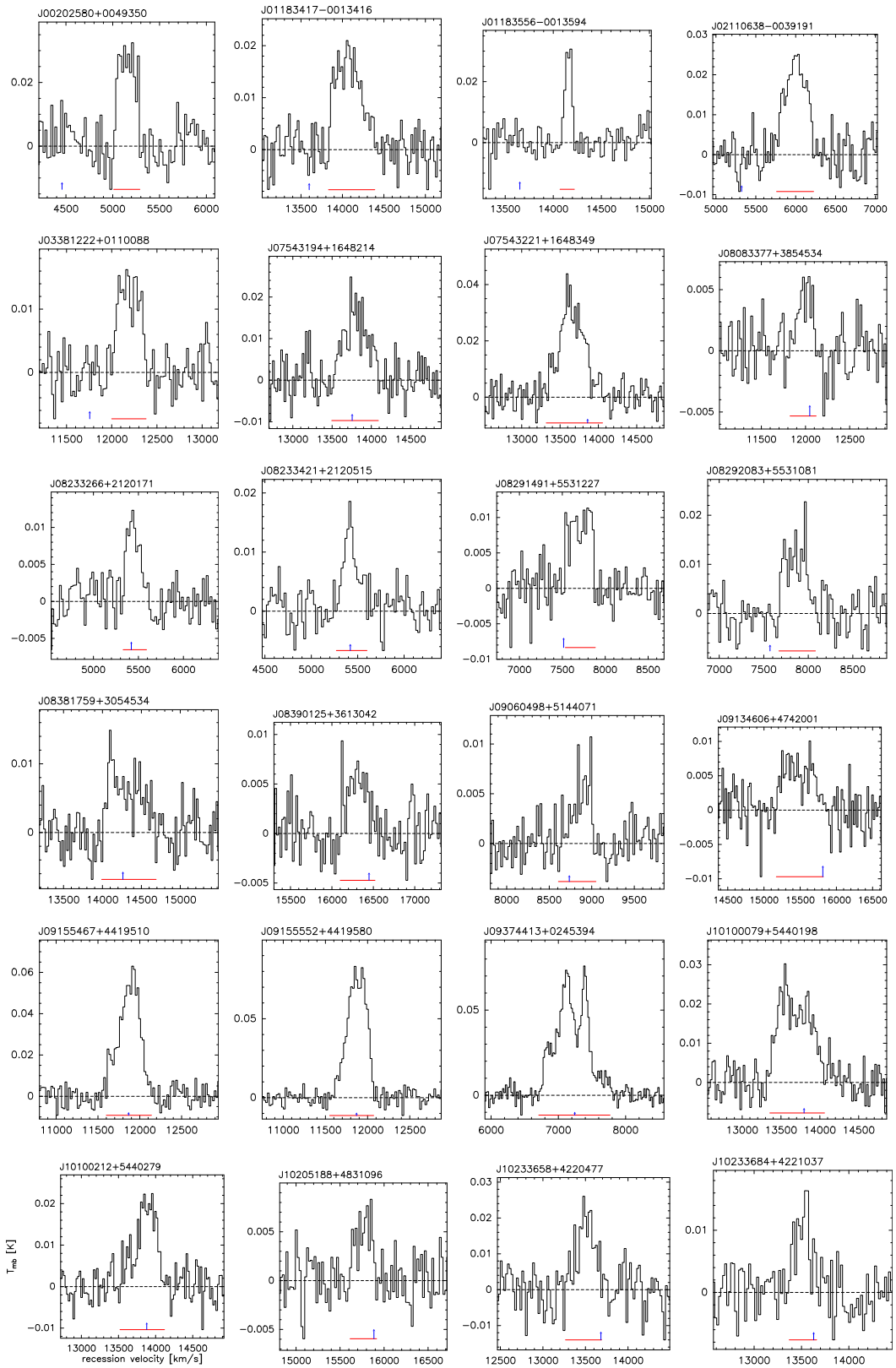

Fig. A.1. CO(1–0) spectra of the detected galaxies (including tentative detections). The velocity resolution is ∼20 km s^{-1} for most spectra and ∼40 km s^{-1} for some cases where a lower resolution was required to clearly see the line. The red line segment shows the zero-level linewidth of the CO line adopted for the determination of the velocity integrated intensity. The blue upright arrow indicated the optical heliocentric recession velocity. An asterisk next to the name indicates a tentative detection.

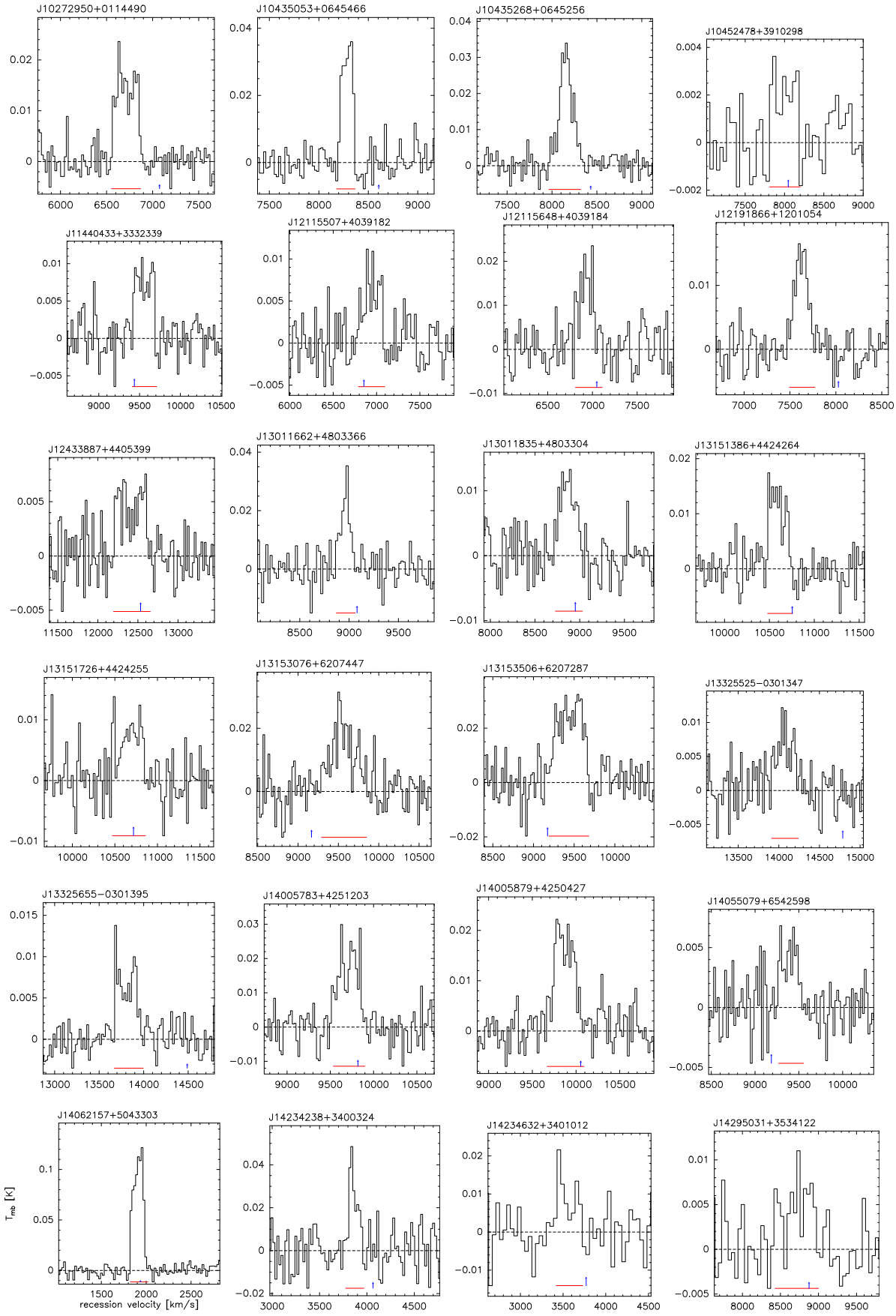

Fig. A.1. continued.

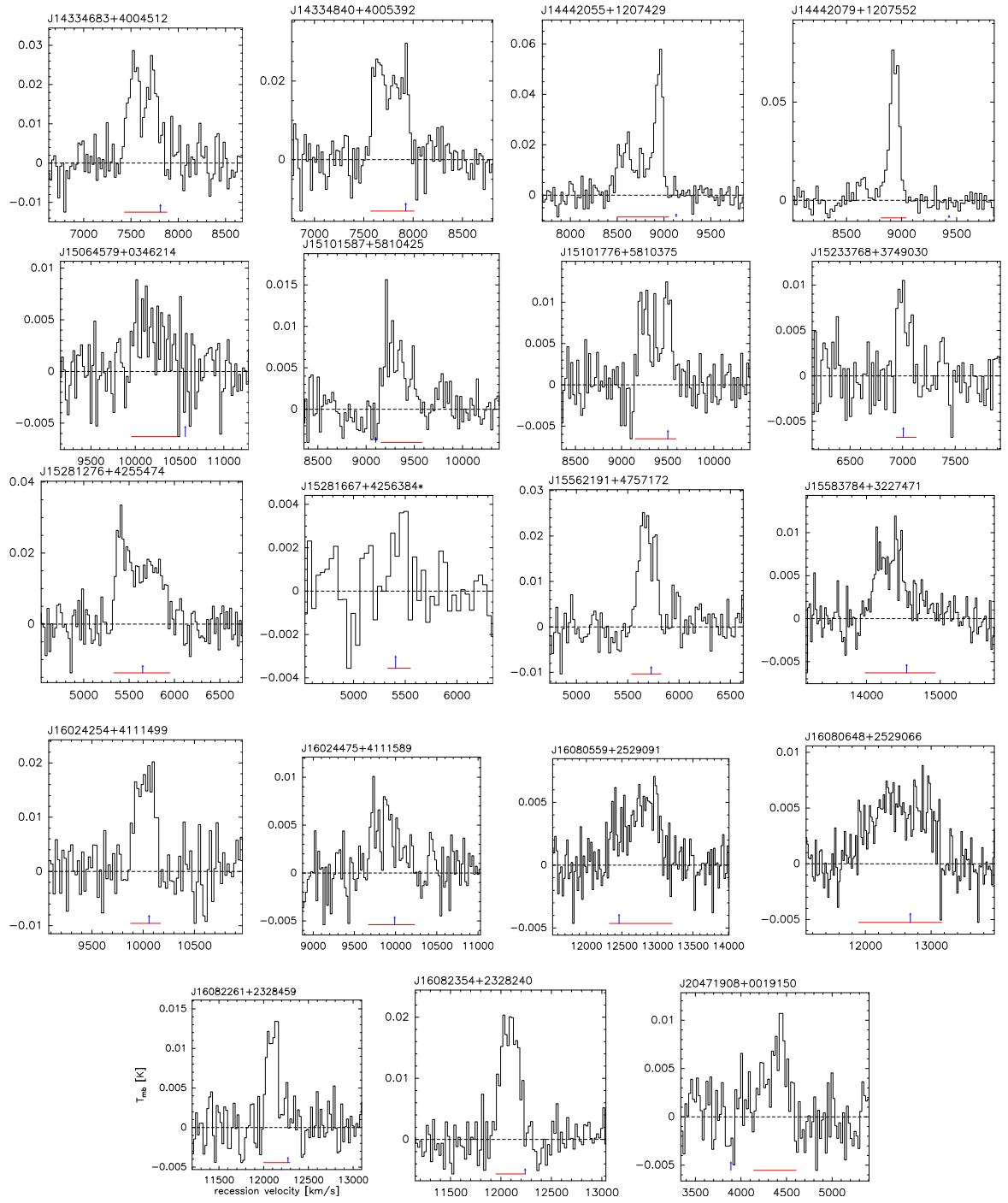

Fig. A.1. continued.

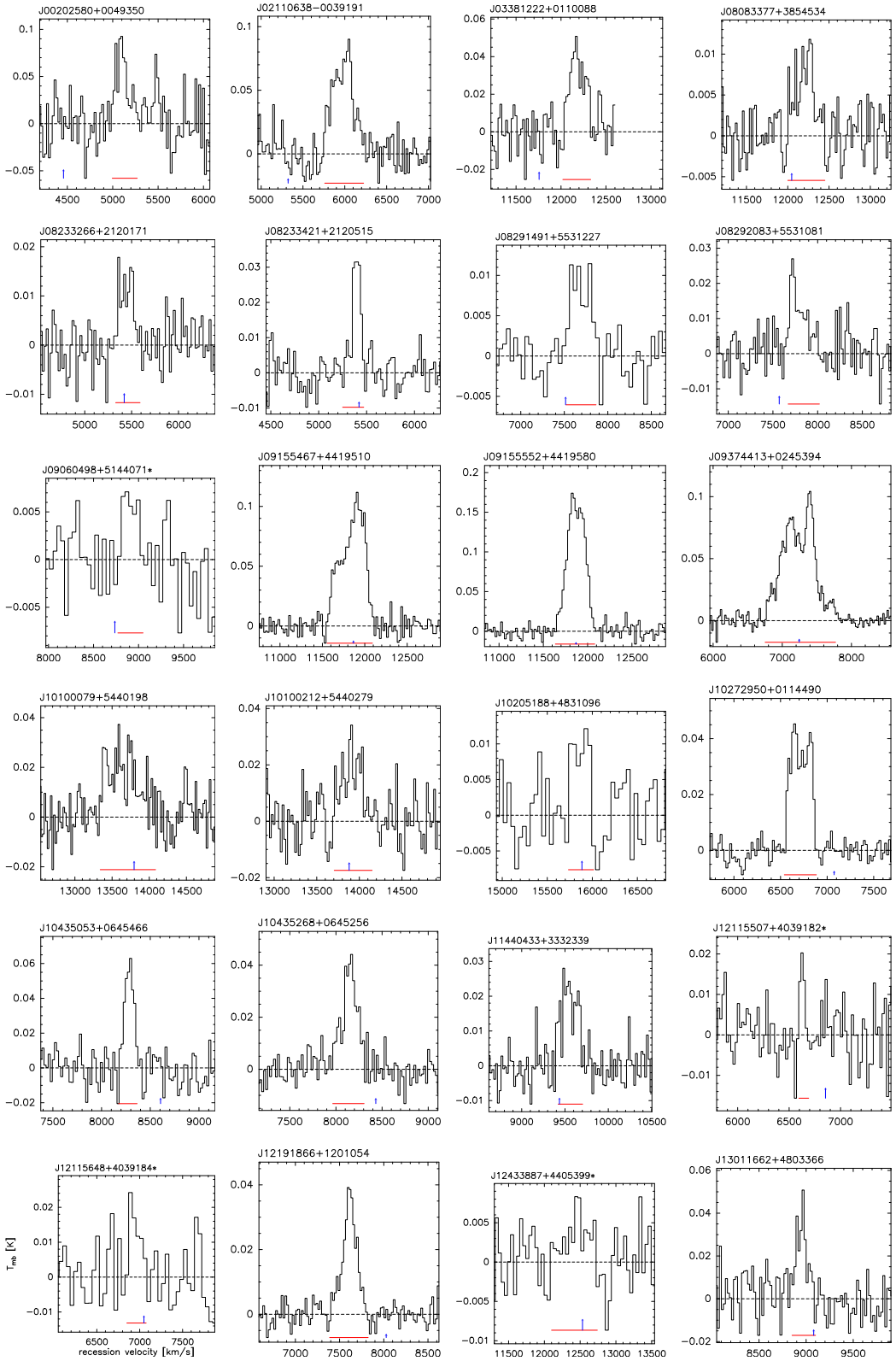

Fig. A.2. CO(2–1) spectra of the detected galaxies (including tentative detections). The velocity resolution is ∼20 km s^{-1} for most spectra and ∼40 km s^{-1} for some cases where a lower resolution was required to clearly see the line. The red line segment shows the zero-level linewidth of the CO line adopted for the determination of the velocity integrated intensity. The blue upright arrow indicated the optical heliocentric recession velocity. An asterisk next to the name indicates a tentative detection.

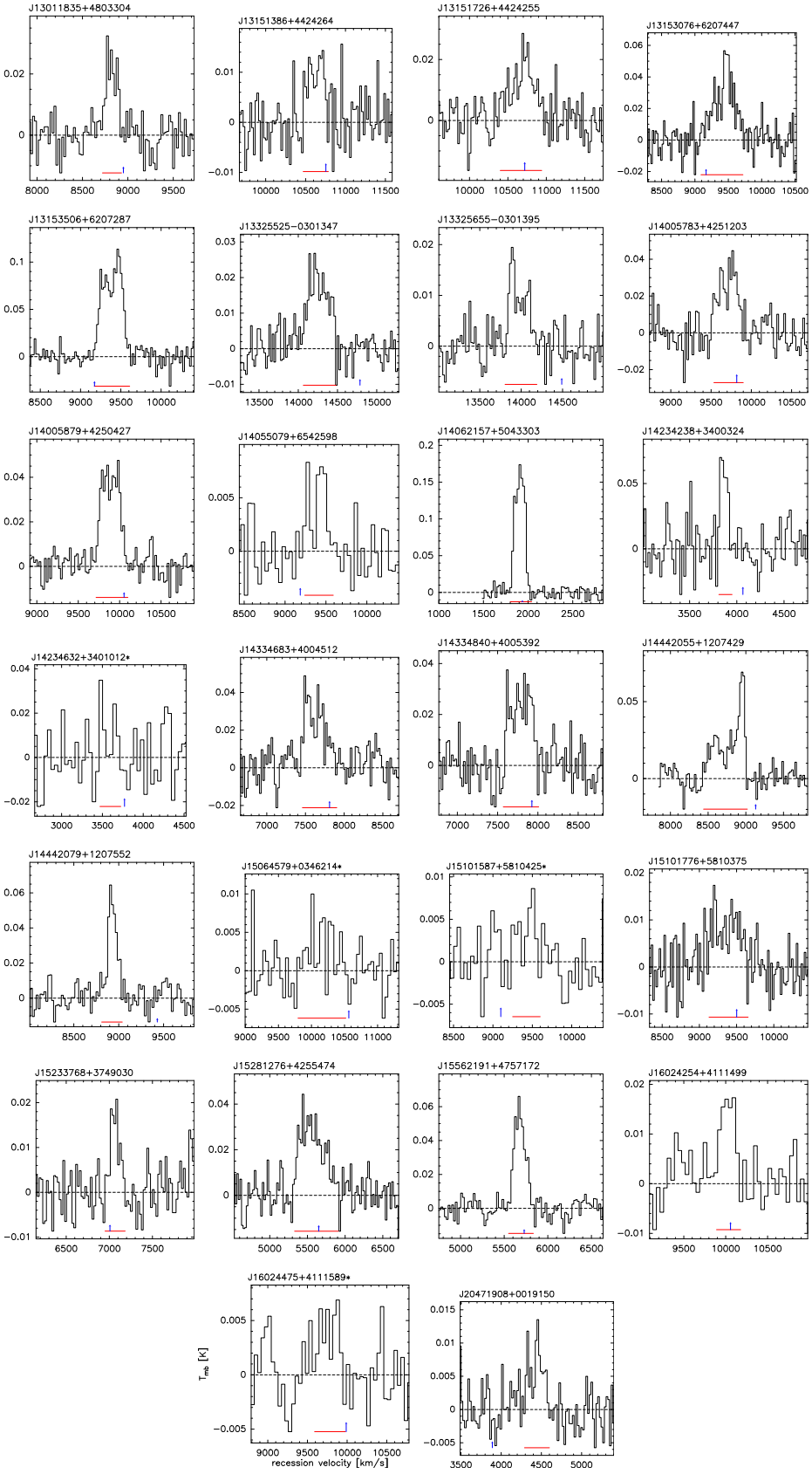

Fig. A.2. continued.